Experimental Evaluation of Microvoid Characteristics and their Relationship with Stress and Strain for Ductile Fracture

Surajit Dey¹, Ravi Kiran² and Chad Ulven³

Abstract

The present study aims to characterize the microvoid sizes and their statistical distribution at the instance of fracture from the fracture surface of steel specimens. To this end, uniaxial tensile tests are conducted on circumferentially notched specimens made of 17-4 PH stainless steel and ASTM A992 high-strength structural steel. The fracture surfaces of the steel test specimens are studied using a digital microscope to quantify the statistical microvoid size distribution. Furthermore, the evaluated microvoid sizes of different fracture locations are mapped with the stress and strain fields. Finally, based on the experimentally evaluated microvoid sizes, an uncoupled fracture model was adopted to predict the fracture displacement and location of ductile fracture initiation in the fractured specimens. The fracture displacements predicted using the calibrated uncoupled fracture model are within the acceptable limit. The fracture initiation locations coincided with the peak strain-averaged stress triaxiality in the fracture specimens.

Keywords: 17-4 PH steel, ASTM A992 steel, Microscopic cup and cones, Void growth model, and Optical digital microscopy

1 Introduction

Ductile fracture is the fracture initiating mechanism in several engineering metals, including stainless steel [1–3], copper [4,5], titanium [6,7], aluminum [8,9], etc. The ductile fracture mechanism can be described as a multi-stage process consisting of void nucleation, void growth, and void coalescence over a critical material volume [10–13]. Microscopic voids originate from pre-existing heterogeneities or material defects present in the form of non-metallic inclusions in the metal matrix. The nucleation of the voids is caused by the decohesion of the non-metallic inclusions from the metal matrix and/or by the cracking of inclusions [14–17]. The nucleated voids elongate and dilate under the influence of the stress state and evolving plastic strain [11]. The stress state is represented by stress triaxiality (T_{σ}), which is the ratio of hydrostatic (mean) stress (σ_h) and Mises (effective) stress (σ_m). Under high-stress triaxiality, the ductile fracture is driven by hydrostatic stress leading to volumetric void growth, whereas ductile fracture under low-stress triaxiality is governed by the Lode parameter resulting in faster elongation and rotation [18–23]. Finally, the microvoids coalesce to form cracks which initiate ductile fracture. Fracture surface of the metal specimens is formed by the coalesced microvoids in the case of ductile fracture, and fractographic studies are of utmost importance to distinguish it from other fracture mechanisms.

Graduate Research Assistant, School of Sustainable Engineering and the Built Environment, Arizona State University, Tempe, AZ, email: sdey34@asu.edu

² Associate Professor (Corresponding author), School of Sustainable Engineering and the Built Environment, Arizona State University, Tempe, AZ, email: ravi.kiran@asu.edu

³ Professor, Mechanical Engineering Dept., North Dakota State University, Fargo, ND 58105, email: chad.ulven@ndsu.edu

Many researchers investigated the role of inclusions in the ductile fracture in nucleating microvoids [16,17,24,25]. Argon and Im [16] conducted an experimental investigation to study the behavior of inclusions with evolving plastic strain in spheroidized 1045 steel, Cu-Cr alloy, and maraging steel. Scanning Electron Microscopy (SEM) micrographs were used to study the inclusion size distribution in the target metals. The fracture surface of the specimens was further observed using SEM to detect the microvoids left on the surface due to debonding of the inclusions. Further, the interfacial strength of equiaxed inclusion particles in the materials was analyzed. Beremin [17] proposed a novel hybrid experimental-analytical method to estimate temperatureindependent local critical stress for void nucleation in A508 class 3 steel with elongated MnS inclusions. Circumferentially notched steel specimens were unloaded after plastic deformation. The unloaded steel specimens were sectioned and polished to examine the elongated MnS inclusions for damage using an optical microscope. The experiments were repeated using three different notch radii for two loading orientations and three testing temperatures. Finally, the local stress and strain at the inclusion locations were mapped using finite element analysis, and critical void nucleation stress was determined using Eshelby's theory for inclusions and inhomogeneities [26]. Later, Le Roy et al. [25] proposed an experimental method to determine void nucleation strain. Smooth tension bars of spheroidized plain carbon steel specimens were pre-strained to various levels and were subsequently heat-treated and reloaded till fracture. The fracture surface of the failed specimens was observed using SEM, and the variation in nucleated void density with evolving macroscopic strain was reported. Pardoen and Delannay [27] used a similar experimental approach to investigate the influence of stress triaxiality on void nucleation strain in circumferentially notched copper bars.

Plateau et al. [28] presented the first fractographic images of dimpled fracture surfaces using SEM. Cox and Low [29] experimentally investigated void growth rates in AISI 4340 and 18 Ni, 200-grade maraging steel. SEM images of the fracture surface of the test specimens were used to quantitatively study the size and spacing of the microvoids. The average spacing between the large dimples was found to be similar to the center-to-center spacings of the dominating nonmetallic inclusions in the materials. The diameter of the large equiaxed dimples on the fracture surface of the maraging steel and AISI 4340 steels ranged between 10 µm to 20 µm and 5 µm to 15 μm, respectively. The void growth rate was found to be larger in notched specimens compared to that of the smooth specimens, which was attributed to the higher stress triaxiality in notched specimens. Floreen and Hayden [30] and Psioda [31] studied the fractographs of 18Ni (280) maraging steel. Floreen and Hayden [30] reported the length and width of the 10 largest microvoids as a function of true strain. Both studies observed the void growth rate to increase with the matrix material strength. Marino et al. [32] conducted a hybrid experimental-analytical study to investigate the void growth rate in powder-processed sintered-forged steel specimens containing alumina particles of volume fractions 0.5% and 2%. The fracture surface of the failed specimens was observed using an optical microscope, and the area of the microvoids was computed. The mean diameter of the alumina particles was found by averaging over 100 particles and was assumed to be the initial void diameter of the material. The void growth rate was found to increase exponentially with the stress triaxiality. Pardoen and Delannay [33] conducted density measurements in copper bars and subsequently derived porosity distribution for the specimens. The global porosity at failure was observed to range between 0.006 to 0.015 for the test specimens.

The annealed specimens with higher hardening capacity were observed to have a lower porosity growth rate compared to that of the as-received specimens.

More recently, Jablokov et al. [34] conducted an experimental investigation of HY-100 notched steel specimens with MnS inclusions. Metallographically polished fracture sections were observed using SEM to extract void area fraction and void density which were presented as a function of the evolving equivalent plastic strain corresponding to different stress triaxiality values. Voids with cross-sectional areas greater than 10 µm² were found to be predominant on the fracture surface of the failed specimens. Chae and Koss [35] conducted a similar experimental investigation on HSLA-100 steel with spherical inclusions. Equiaxed voids with a major dimension greater than 10 µm were predominant on the fracture surface. The void area fractions corresponding to the ductile fracture initiation for different stress triaxialities were found to be ranging from 0.003 to 0.008. Benzerga et al. [36] experimentally investigated void size and porosity in X-52 medium carbon low alloy steel. Void sizes were measured from the fracture surface of the notched test specimens using SEM images. Further, local porosities were estimated using Dirichlet cell analysis, and critical porosity for void coalescence was determined. The critical porosities for longitudinal and transverse loading were approximately 0.02 and 0.01, respectively. The void growth rate was found to be the largest at the center of the specimens. Further, the void growth ratios were observed ranging between 3 and 10 for longitudinal loading, whereas for transverse loading, void growth ratios lie between 2 and 50. More recently, with the development of X-ray tomography progressive damage in materials can be observed directly without destructive evaluation of the test specimens [37–42].

Although there exist a few microscopic studies that investigated the microvoid characteristics in metals at fracture, the following research questions remain unanswered: (a) how to characterize the sizes of microvoids from the fracture surface? (b) what is the statistical distribution of the microvoid sizes present on the fracture surface of steels at failure? and (c) how to validate the experimentally evaluated microvoid sizes? This paper addresses these research questions and is organized as follows: Section 2 presents the materials used, geometric details of the test specimens, and the details of the uniaxial tension tests conducted. Furthermore, the experimental protocol adopted for optical microscopy of the fracture surfaces and the statistical analysis of the microvoids present on the ductile fracture surface is also discussed. In Section 3 the details of the finite element model used to extract the stress and strain states of the test specimens are presented. The stress triaxiality and equivalent plastic strain variation across the cross-section of the notched specimens are also discussed. The relationship between the experimentally evaluated microvoid size and the state of stress and strain in the test specimens is also presented. Furthermore, the relationship is validated using the experimental results. Finally, Section 4 provides the contributions and important conclusions drawn from the present study.

2 Fracture Tests and Microvoid Analysis

Uniaxial tension tests were performed on circumferentially notched steel specimens followed by optical microscopy of the fracture surfaces. This section provides details of the mechanical testing protocol and the geometry of steel test specimens. Furthermore, the procedure

for the optical microscopy analysis of fracture surfaces along with the assumptions made for the evaluation of microvoid statistics will be discussed.

2.1 Metals Investigated: 17-4 PH steel and ASTM A992

Uniaxial tensile tests were conducted on circumferentially notched cylindrical specimens made of 17-4 PH stainless steel and ASTM A992 high strength low alloy (HSLA) steel. 17-4 PH stainless steel and ASTM A992 steel are used in this study for their wide engineering applications. 17-4 PH stainless steel has applications in aerospace, petrochemical, nuclear, and defense industries due to ease of fabrication, corrosion resistance, high strength, and ductility [43]. ASTM A992 is a structural steel that is preferred for higher yield strength, yield-to-tensile strength ratio, weldability, fracture toughness, and quality control [44]. ASTM A992 steel is widely preferred in the United States for wide-flange structural steel sections used in steel structures [45,46]. The mechanical properties of both steels can be in part attributed to their chemical composition. The chemical compositions of both the steels are summarized in Table 1. 17-4 PH stainless steel contains 15-17.5 wt.% chromium which contributes towards the corrosion resistance in an aqueous environment due to the formation of a passivating oxide film [47]. Moreover, 17-4 PH stainless steel derives a significant part of its strength from precipitation reactions. For ASTM A992 steel, the carbon content is limited to 0.15 wt.% which results in reduced carbon equivalent (CE) and in turn improves the weldability of steel [44]. The high strength of ASTM A992 steel is obtained by using alloying elements such as vanadium, manganese, columbium, and molybdenum. Furthermore, chromium contributes towards the corrosion resistance and nickel enhances the fracture toughness of ASTM A992 steel.

Microstructure also contributes to the favorable mechanical properties of steel. The microstructure of both the steel specimens was studied using disc-shaped steel specimens which were prepared and subsequently ground using silicon carbide (SiC) paper in the following order of grit size: 60, 120, 400, 800, and 1200. The disc-shaped steel specimens were further polished using alumina suspension. Finally, the polished ASTM A992 steel and 17-4 PH stainless steel specimens were etched using 2% Nital solution and Fry's reagent (CuCl₂, HCl, and distilled water), respectively, to reveal the microstructure of the material and were observed using a light microscope. The microstructure of the etched 17-4PH stainless steel and ASTM A992 structural steel specimens are presented in Figure 1. As shown in Figure 1(a), 17-4 PH stainless steel microstructure is primarily dominated by martensite which is characterized by needle-shaped microstructural features [48]. The microstructure of ASTM A992 structural steel is composed of ferrite and pearlite [49]. Ferrite is a body-centered cubic structure phase of iron whereas pearlite consists of alternating layers of two microstructural phases namely, cementite and ferrite. The microstructure phases in ASTM A992 structural steel are labeled in Figure 1(b) where the light-colored grains represent the ferrite phase and the dark-colored grains represent the pearlite phase.

2.2 Fracture Specimens and Testing

In the present study, two different notch shapes were tested to achieve high stress triaxilities. Specimens that produce stress triaxialities greater than 0.45-0.67 are usually referred to as high triaxility specimens based on the literature [20]. Microvoid dilation leading to coalescence is the dominant damage mechanism at high stress triaxilities [50,51]. Hence, it will be

possible to use the microvoid information from the fracture surface to predict the fracture of steel. The fracture specimens in this study are designated as circular notch (CN) and U-shaped notch (UN). The geometric details of these notched specimens along with the reference unnotched specimen (RU) are provided in Figure 2. The dimensions of the test specimens and notches used to achieve initial triaxilities between 0.33 and 0.94 (see Section 3 for FE analysis) are provided in Table 2. All the test specimens were machined using a computer numeric control (CNC) lathe machine with a tolerance of \pm 0.025 mm. The test specimens were subjected to a uniaxial tensile load using a servo-hydraulic MTS 809 system with a displacement rate of 0.02 mm/sec and the strains were recorded using a contact extensometer with a 1-inch gauge length (Epsilon Model 3542).

2.3 Optical Microscopy

Optical microscopes are widely used to study surface topography with applications in manufacturing, healthcare, biology, and geology among others [52–58]. An optical microscope is equipped with white light which is projected on the test specimen. For translucent or opaque objects, the light is reflected off the surface of the specimen whereas the projected light beam passes through the specimen for transparent or semi-transparent objects. Upon projection of the white light, the reflected/ refracted light is received using a series of optical lenses (optics) which help in the 3D reconstruction of the surface of the test specimen. Depending on the focal length, optical lenses of different magnifications are available which help in magnifying the small features present on the surface of the test specimen. In the present study, the purpose of an optical microscope is two-fold: (a) to capture the macroscopic image of the fracture surface of the failed steel test specimens, and (b) to obtain the magnified images of different locations on the fracture surface to quantify microvoid characteristics. The white light provided in an optical microscope has a wavelength ranging from 390 to 760 nm which theoretically provides the capability of capturing features at a length scale of $\sim 0.2~\mu m$ depending on other factors such as wavelength and refractive index of the specimen and the medium [59].

Although theoretically possible, conventional optical microscopes are not capable of resolving features at the micro-scale, thus, making them suitable for only capturing macro-scale images of the fracture surface. Therefore, traditionally the magnified images of different regions on the fracture surface of the failed test specimens are captured using SEM. However, SEM study of the test specimens involves certain shortcomings. Although SEM provides high-resolution micrographs, most scanning electron microscopes can provide only grey-scale 2D micrographs, which constrains microscopic analysis of the surface of test specimens. Moreover, many of the stop-cut-see studies involving SEM analysis involve sectioning and polishing of test specimens which may cause void smearing leading to errors in the analysis [13]. The present study involves the characterization of microvoids in the form of dimples present on the fracture surface of steel specimens that have undergone ductile fracture. The fracture surface of the failed steel specimens consists of an uneven topography due to the presence of dimples on the surface. Therefore, color 3D reconstructed micrographs would aid in deciphering the dimple boundaries and minimizing errors in quantifying microvoid dimensions on the fracture surface. With the recent development of image sensors and optical systems, advanced digital microscopes are now capable of capturing high-resolution micrographic features at a length scale of ~1 µm.

In the present study, a Keyence VHX 7000N digital microscope was used to capture micrographs of the fracture surface of the steel test specimens. The digital microscope is equipped with a 4K complementary metal oxide semiconductor (CMOS) image sensor and a newly developed NEO REMAX imaging engine which help in providing high-resolution images coupled with a large depth of field (~20 times greater than conventional optical microscopes). Furthermore, the microscope is also provided with high-resolution (HR) objective lenses capable of providing magnifications ranging from 20X (length scale of ~1 mm) to 2500X (length scale of ~1 μm). The macroscopic images of the fracture surface of the steel test specimens were observed using magnification ranging between 20X-80X. Figure 3 and Figure 4 present the macroscopic fracture images of 17-4PH stainless steel and ASTM A992 steel specimens, respectively. The reference unnotched specimen RU for both the steels experienced significant necking resulting in a typical macroscopic cup-and-cone fracture. This can be attributed to the low stress triaxiality during the initial straining phase in the unnotched specimens allowing necking before fracture. However, the notched steel specimens have higher initial stress triaxiality compared to that of the unnotched reference specimens. This aids in earlier microvoid initiation in the notched specimens leading to fracture prior to necking compared to that of the unnotched specimens. Furthermore, highresolution magnified images of various locations on the fracture surface of the test specimens were also captured using the digital microscope which will be discussed in the following section.

2.4 Microvoid Characterization and Statistics

Ductile fracture is characterized by the presence of dimples and these visual features are of interest in this study. The sizes of the dimples depend on the magnitude of the stress concentration and the extent of plastic flow in the material at the instance of fracture. Usually, the size of these dimples ranges between a few microns to tens of microns. One of the motives of this paper is to quantify the microvoid size statistics from the micrography studies on the fracture surfaces. To this end, firstly, the fracture surface of each of the test specimens was divided into three distinct zones between the center and periphery of the cross-section. The cross-section is divided into different zones to account for the lack of uniformity in the stress and strain state across the cross-section during the deformation process (see Figure 5 and Figure 6) [45,50]. The number of zones is limited to three so that enough fracture surface area would be available to conduct the statistical sampling of microvoids. Zone-1 (regions 1 & 5) and Zone-2 (regions 2 & 4) have two regions each, unlike Zone-3 (region 3), owing to the symmetry of the fracture surfaces (see Figure 7 and Figure 8).

To get a clear and close glance at the dimples, magnification ranging between 500X-1000X was employed. The magnified high-resolution images of different regions on the fracture surface of reference unnotched specimen (RU) made of 17-4 PH stainless steel and ASTM A992 structural steel are presented in Figure 7 and Figure 8, respectively. The high-resolution micrographs of each of the fracture zones were used to compute microvoid areas using the image analysis software ImageJ [60]. The microvoid analysis is based on two assumptions: 1) the microvoids at coalescence are approximately spherical, and 2) each fracture surface contains approximately one-half of the spherical void. However, in reality, the pits on the fracture surface are not perfectly circular. Hence, their projected area is evaluated first and then the equivalent radii are calculated assuming the extracted cross-section geometry to be circular. An experimental protocol was

established for extracting the microvoid areas which is discussed further. Two separate $75\mu\text{m}\times75\mu\text{m}$ areas were randomly drawn on the micrograph of each of the five regions in the three zones (see Figure 9). The choice of the $75\mu\text{m}\times75\mu\text{m}$ area for microvoid analysis is based on the typical sizes of dimples which ranged between 0.5-4 μm . In other words, if a line is drawn parallel to one of the sides of this area, about 10-75 dimples are encountered. To minimize the analysis time and to avoid redundant data, 25 microvoids were sampled that are representative of all the different sizes of microvoids present in the area drawn on the fracture surface of the test specimen.

The histograms of void size (equivalent radii) distributions of the three distinct fracture zones extracted from the micrographs of 17-4 PH stainless steel and ASTM A992 structural steel test specimens are presented in Figure 10 to Figure 12. To determine the nature of the void size distribution present on the fracture surface of the test specimens, statistical analysis was performed on the experimentally extracted void size (equivalent radii) data. Based on the statistical analysis, the void size (equivalent radii) distributions were observed to follow an approximately normal distribution. In addition to histogram plots, normal probability plots are also used as a graphical technique to identify departures from normality. The normal probability plots showing the variation in theoretical Z-score with the experimentally extracted equivalent microvoid radii are presented in Figure 13 to Figure 15. The extracted equivalent void radii corresponding to the different fracture zones of all the specimens were found to approximately follow a linear pattern in the normal probability plots with slight deviations at the ends. Furthermore, Skewness and Kurtosis of the equivalent void radii distributions for all the test specimens were also evaluated. Skewness measures the degree of symmetry in the data distribution whereas Kurtosis captures the presence of outliers in the data. The Skewness and Kurtosis measures of the distributions are reported in Table 3 and Table 4, where the values range between -1 and +1. The histogram and normal probability plots indicate that the void size distributions of all the test specimens approximately follow the gaussian distribution like many other natural phenomena which provides more confidence about the sample size of equivalent microvoid radii extracted from the micrographs of the fracture surface of the steel test specimens.

The deviations in the normal probability plots can be attributed to the slightly heavy tail observed in the histogram plots. As a result of these deviations, the mean equivalent microvoid radius corresponding to the majority of the void size (equivalent radii) distributions was observed to be greater than that of the median equivalent microvoid radius, thereby indicating that the distributions are slightly right-skewed. The positive skewness in the void size distributions might have resulted from the coalescence of microvoids on the fracture surface of the steel test specimens. Furthermore, the right-skewed void size distribution implies that the larger coalesced voids formed in the fracture zones during the straining of the test specimens significantly influence the mean equivalent microvoid radius of the void size distributions. Presently, the authors do not have evidence to identify the range of microvoid sizes that are responsible for ductile fracture initiation and propagation in the steel test specimens and further analysis needs to be conducted in the future.

The mean (μ) and standard deviation (σ) of the microvoid sizes corresponding to each of the fracture zones of the test specimens are reported in Figure 10 to Figure 12. In addition, the median $(\mu_{1/2})$ of the extracted experimental microvoid size data is also reported. For the 17-4 PH steel specimens CN2, CN3, and RU the mean equivalent microvoid radius was observed to be the least at the periphery (Zone-1) and largest at the center of the fracture surface (Zone-3), implying that fracture might have initiated at the center [36,50]. Furthermore, the standard deviation of the equivalent microvoid radii was found to be the least for voids in the fracture Zone-1 (periphery) of these test specimens. This could imply one or two of these scenarios: 1) the microvoid growth was more uniform near the periphery compared to the center of the fracture surface and/ or 2) there are no new smaller secondary voids near the periphery. It should be noted that the secondary voids originate at a later stage in the deformation process and are usually smaller than the voids that originated from larger defects or voids that nucleated earlier. At this stage, the authors do not have experimental evidence to conclude either of the above scenarios. For 17-4 PH specimen CN1, the mean equivalent microvoid radius corresponding to Zone-2 was found to be the largest implying that fracture might have initiated from the fracture region located in between the center and periphery of the fracture surface. Furthermore, the standard deviation for void size was lowest at the periphery (Zone-1) and highest at the fracture Zone-2, leading to greater non-uniformity in void sizes at the zone of fracture initiation.

For ASTM A992 structural steel specimens CN4, CN5, and RU, the mean equivalent microvoid radius was largest for the fracture Zone-3, implying that ductile fracture might have initiated at the center of the test specimens. The standard deviation of the void size distributions of specimens CN4, CN5, and RU were observed to be highest at Zones-2, 3, and 1, respectively, implying greater non-uniformity of void size possibly due to the presence of secondary voids. In the case of ASTM A992 specimen CN2, the highest mean equivalent microvoid radius was observed at fracture Zone-1, thereby indicating that ductile fracture might have initiated near the periphery of the fracture surface. For specimen CN2, the standard deviation of the equivalent microvoid radius was observed to be the largest at Zone-2 of the fracture surface. In the case of specimen UN, the highest mean equivalent microvoid radius was observed at Zone-2, implying that ductile fracture initiated between the center and periphery of the fracture surface. The highest standard deviation of the void size distribution was observed at Zone-3, implying the largest variation in microvoid size at the center of the fracture surface.

3 Relationship between Void Sizes and Stress and Strain States

3.1 Evaluating Stress and Strain Fields

Non-linear finite element analysis was conducted on cylindrical tensile test specimens using a commercially available finite element program ABAQUS[®] [61]. The test specimens were discretized using four-node bilinear axisymmetric CAX elements with hourglass control available in the ABAQUS element library. A typical finite element model along with the employed boundary conditions is presented in Figure 16. The material non-linearity was captured by using the J_2 plasticity model available in the finite element program. Furthermore, the geometric non-linearity of the test specimens was also considered in the finite element solutions. The strain hardening

curves used for the finite element model were extracted from the uniaxial tension test on reference unnotched specimens and are presented in Figure 17. A finite element mesh size of 0.025 mm was used to capture the stress and strain fields in the critical regions. It is important to note that the dimension of the area $(75\mu\text{m}\times75\mu\text{m})$ drawn on the micrographs for extracting the microvoid areas was chosen such that it is sufficiently larger than the size of the finite element mesh.

The load-displacement response obtained from the finite element models was in good agreement with that of the experimental results until the peak load-carrying capacity of the test specimens. A comparison between the predicted and experimental load-displacement response of 17-4 PH stainless steel and ASTM A992 high-strength structural steel specimens is presented in Figure 18 and Figure 19, respectively. The experimental load-displacement curves of the test specimens descend rapidly after attaining the peak load-carrying capacity, whereas the post-peak branch of the finite element predicted curve is more gradual compared to that of the experimental observation. The post-peak mismatch between the experimental observation and the predicted curve can be attributed in part to the inability of the J_2 plasticity model in capturing the damage caused by the microvoid growth and coalescence.

The stress-strain fields were extracted from the non-linear finite element analysis performed on the cylindrical tension test specimens. The stress triaxiality variation with respect to the normalized radius at the initial loading stage and corresponding to fracture for 17-4 PH stainless steel and ASTM A992 steel are presented in Figure 5 and Figure 6, respectively. Owing to the stress flow discontinuity caused by the notches, the stress triaxiality corresponding to the initial stage of loading attains a maximum near the notch root, whereas the stress triaxiality for the unnotched specimens remains largely constant. In the case of ASTM A992 structural steel specimens, the maximum initial stress triaxiality ranges between 0.33 and 0.94, whereas the maximum stress triaxiality at fracture ranges between 0.54 and 1.17. For 17-4 PH stainless steel specimens, the maximum initial stress triaxiality varies from 0.33 to 0.82, whereas the maximum final stress triaxiality ranges between 0.83 and 1.54. Furthermore, the variation of equivalent plastic strain at fracture with respect to the normalized radius for 17-4 PH stainless steel and ASTM A992 structural steel specimens are presented in Figure 20.

The stress-strain field variations extracted from the finite element models indicate that the stress triaxiality evolves over time during the deformation process. Therefore, to capture the variation in stress triaxiality over the entire loading history, strain-averaged stress triaxiality (\bar{T}_{σ}) was computed which will be used for validating the experimental microvoid sizes. The strain-averaged stress triaxiality is defined as:

$$\bar{T}_{\sigma} = \sum_{i=1}^{n} \frac{(T_{\sigma})_{i} \Delta \varepsilon_{p}}{\varepsilon_{p}} \tag{1}$$

where, $(T_{\sigma})_i$ is the stress triaxiality corresponding to the i-th loading step; $\Delta \varepsilon_p$ is the plastic strain increment corresponding to the i-th step; ε_p is the equivalent plastic strain at fracture; n is the total number of steps. The strain-averaged stress triaxiality variation with respect to the normalized radius for 17-4PH stainless steel and ASTM A992 high-strength steel test specimens are presented in Figure 21.

3.2 Validation of the Experimentally Evaluated Microvoid Sizes

If the experimentally evaluated microvoid sizes are accurate, existing fracture models can be calibrated from this information to accurately predict fracture initiation in models that rely on the critical void size at fracture. Although the Gurson model [62] and its extensions [63–67] are popularly used for predicting fracture, they have parameters such as initial void volume, critical void volume, etc., which cannot be evaluated in the current study. For this reason, the void growth equation proposed by Rice and Tracey [68] is considered in this study. Rice and Tracey [68] analytically derived an expression for the growth of a single spherical void in a plastic material under high stress triaxiality which is given as

$$\frac{dR}{R} = \alpha exp\left(\frac{\beta \sigma_h}{\sigma_V}\right) d\varepsilon_p \tag{2}$$

where R is the radius of the spherical void, σ_h is the hydrostatic stress, σ_Y is the yield stress; and $\varepsilon_p = \sqrt{2/3} \| \varepsilon_p \|$ where ε_p is the equivalent plastic strain and ε_p is the plastic strain tensor. The parameters α and β are 0.283 and 1.5, respectively. This model is widely used as the Rice and Tracey void growth model (VGM). D'Escata and Devaux [69] incorporated hardening in the original void growth equation by replacing yield stress (σ_Y) with Von-Mises stress (σ_m) . Thus, the modified VGM growth equation is given as

$$\int \frac{dR}{R} = \int_0^{\varepsilon_p} \alpha exp(\beta T_\sigma) d\varepsilon_p \tag{3}$$

Hancock and Mackenzie [70] assumed that the stress triaxiality (T_{σ}) is largely unchanged throughout the straining process and proposed the stress modified critical strain model (SMCS). The SMCS model considers the instantaneous stress triaxiality at fracture and hence may not predict ductile fracture initiation accurately [50,71,72]. Therefore, to incorporate the stress history effect in the SMCS model, the stress triaxiality (T_{σ}) is replaced with strain-averaged stress triaxiality (\bar{T}_{σ}) in the present study. Thus, the modified SMCS model is expressed as

$$\ln(R) = \ln(R_0) + \alpha exp(\beta \bar{T}_\sigma) \varepsilon_p \tag{4}$$

where, R_0 is the radius of the initial void present in the material.

R is the equivalent radius of the microvoids present on the fracture surface of the failed test specimens. The mean microvoid equivalent radius corresponding to the distinct fracture zones of all the test specimens was extracted from the high-resolution micrographic images using ImageJ. Each fracture zone is assumed to span over approximately one-tenth of the radius of the test specimens based on the scale of the extracted microscopic images of the fracture zones. Therefore, the strain-averaged triaxiality and the equivalent plastic strain values were averaged over one-tenth of the radius present in each of the distinct fracture zones. The span of each of the fracture zones was ~10 times the size of the finite element mesh and ~250 times the minimum microvoid size (equivalent radius) observed on the fracture surface of the steel test specimens. As shown in Figure 22, the \bar{T}_{σ} and ε_{p} values for Zone 1 are averaged between normalized radii 0 and 0.1, Zone 2 between normalized radii 0.45 and 0.55, and Zone 3 between normalized radii 0.9 and 1. The average equivalent void radius, strain-averaged triaxiality, and effective plastic strain

corresponding to each fracture zone for all the test specimens were computed. Subsequently, these values were substituted in Eq. 4, and using the Gauss-Newton method for non-linear regression [73] the parameters R_0 , α , and β were computed. Following this, the critical plastic strain (ε_p^{cr}) was obtained by substituting the experimentally obtained average equivalent void radius and the computed parameter values and can be expressed as

$$\varepsilon_p^{cr} = \frac{[\ln(R) - \ln(R_0)] \exp(-\beta T_\sigma)}{\alpha} \tag{5}$$

In the present study, an uncoupled damage criterion was presented for 17-4 PH stainless steel and ASTM A992 high strength steel. The flowchart of the proposed methodology for calibrating the failure criterion for steels is presented in Figure 23. Eq. 5 forms the basis of the failure criterion used in the present study. The parameter values for computing the critical plastic strain (ε_p^{cr}) were calibrated using the experimental and numerical data from all the tested 17-4 PH stainless steel and ASTM A992 steel specimens and are presented in Table 5. Based on the parameter R_0 predicted by the fracture criterion, the mean equivalent radii of the primary microvoids present in the untested 17-4 PH stainless steel and ASTM A992 high-strength steel specimens were observed to be 27% and 15% smaller compared to that of the tested specimens, respectively. The $(\varepsilon_p - \varepsilon_p^{cr})$ profiles for the 17-4 PH stainless steel and ASTM A992 structural steel specimens are presented in Figure 24 and Figure 25, respectively. Ductile fracture is assumed to have initiated in the steel specimens when the equivalent plastic strain extracted from the finite element models exceeds the critical plastic strain over a critical length defined as the characteristic length (l^*) of the material [50,71]. The characteristic length (l^*) was obtained by assessing the $(\varepsilon_p - \varepsilon_p^{cr})$ profiles of all the test specimens corresponding to the fracture strain and the lowest length over which the equivalent plastic strain exceeds the critical plastic strain was adopted as the characteristic length for the steel in consideration. The characteristic lengths of 17-4 PH stainless steel and ASTM A992 structural steel are 50 µm and 75 µm, respectively.

The proposed methodology was validated by comparing the predicted fracture displacement (Δ_{Pre}) with the experimentally observed fracture displacement (Δ_{Exp}). Table 6 presents the comparison between the predicted and experimentally observed fracture displacements for the steel test specimens. The model yielded conservative predictions of the fracture displacements which are within the acceptable range. It is important to note that the parameters for computing the critical plastic strain were obtained based on the mean equivalent radius of the microvoids present in the individual fracture zones of the test specimens. However, the larger coalesced microvoids dictate the ductile fracture initiation in steel and were observed to significantly influence the mean equivalent void radius of the different fracture zones of the test specimens resulting in right-skewed void size distributions. Therefore, the conservative fracture displacements predicted by the failure criterion can be attributed to the use of average equivalent microvoid radii in computing the critical plastic strain for the steel test specimens. Furthermore, the fracture criterion was also used to predict the location of ductile fracture initiation in the steel test specimens. As discussed earlier, ductile fracture is assumed to initiate when the equivalent plastic strain in the specimen exceeds the critical plastic strain over the characteristic length of the

material which can be tracked using the $(\varepsilon_p - \varepsilon_p^{cr})$ profiles presented in Figure 24 and Figure 25. For 17-4 PH stainless steel, the equivalent plastic strain exceeded the critical plastic strain over the characteristic length of 50 um at the center of the cross-section for specimens CN2, CN3, and RU (see Figure 24), implying that ductile fracture initiated at the center (Zone-3) which coincided with the locations of the peak strain-averaged stress triaxiality (see Figure 21) and the highest mean equivalent microvoid radius (see Figure 10). In the case of 17-4 PH specimen CN1, the critical plastic strain was exceeded over the characteristic length of 50 µm (see Figure 24) at Zone-1 implying that ductile fracture initiated near the periphery which coincided with the location of peak strain-averaged stress triaxiality (see Figure 21). The highest mean equivalent microvoid radius was found at fracture Zone-2 (see Figure 10) for specimen CN1. For ASTM A992 high strength steel, ductile fracture was predicted to initiate at the center of the cross-section (Zone-3) for specimens CN4, CN5, and RU (see Figure 25) which coincided with the locations for peak strain-averaged stress triaxiality (see Figure 21) and highest mean equivalent microvoid radius (see Figure 11 and Figure 12). For ASTM A992 specimen CN2, the ductile fracture initiation was predicted near the periphery (see Figure 25) which is consistent with the locations of the peak strain-averaged stress triaxiality (see Figure 21) and highest mean equivalent microvoid radius (see Figure 11). The critical plastic strain was exceeded near fracture Zone-2 over the characteristic length of 75 µm for ASTM A992 specimen UN (see Figure 25). The peak strain-averaged stress triaxiality (see Figure 21) and mean equivalent microvoid radius (see Figure 11) coincided with the predicted location of ductile fracture initiation for specimen UN. Therefore, the observations made from the $(\varepsilon_p - \varepsilon_p^{cr})$ profiles, strain-averaged stress triaxiality profiles, and the void size distributions indicate that the highest strain-averaged stress triaxiality and the mean equivalent microvoid radius can act as indicators of ductile fracture initiation location in steels. Furthermore, the locations of the highest mean equivalent microvoid radius and predicted ductile fracture initiation coincide for most of the test specimens implying that larger microvoids significantly influence ductile fracture initiation in steel.

4 Conclusions

The following conclusions can be drawn from the present study:

- 1) The microvoid radii observed on the fracture surfaces range between 0.89 μm and 3.91 μm for 17-4 PH stainless steel, whereas the microvoid radii range for ASTM A992 structural steel is between 1.04 μm and 3.45 μm .
- 2) The void size distributions for the individual fracture zones were observed to approximately follow a normal distribution with a positive skew. Furthermore, 95 percent of the void radii fall between 0.95 μ m to 3 μ m for 17-4 PH stainless steel specimens, whereas 95 percent of the void radii lie between 1.23 μ m to 2.92 μ m for ASTM A992 steel specimens.
- 3) The initial void sizes are estimated after calibrating the uncoupled fracture model. The initial average microvoid radius for 17-4 PH stainless steel and ASTM A992 high strength steel was found to be approximately 27% and 15% smaller than the final average microvoid radius, respectively.

- 4) The extracted microvoid radii were used to calibrate an uncoupled fracture criterion to validate the experimentally extracted void radii. The calibrated uncoupled fracture criterion was used to predict the fracture initiation displacement of the test specimens. The calibrated fracture criterion was able to yield conservative estimates of fracture displacement with a maximum error of 13.6% and 11.1% for ASTM A992 and 17-4PH stainless steel test specimens, respectively. The conservative estimates of fracture initiation displacement using the uncoupled fracture model can be attributed to the use of average microvoid size (equivalent radius) of the individual fracture zones of the test specimens to compute the critical plastic strain whereas, in reality, ductile fracture initiation is dictated by the larger coalesced microvoids and not by the mean void sizes.
- 5) The fracture criterion was also used to plot $(\varepsilon_p \varepsilon_p^{cr})$ profiles for all the test specimens which aid in identifying the location of ductile fracture initiation in the steel specimens. In this study, the location corresponding to the highest mean void size (equivalent radius) is considered to be the fracture initiation location as ductile fracture initiates due to the coalescence of large voids at high triaxiality. The location of ductile fracture initiation was observed to coincide with the location of peak strain-averaged stress triaxiality which can act as an indicator of ductile fracture initiation location in steel.

Acknowledgement

The research presented in this presentation was supported by the National Science Foundation under CAREER award # 2045538. Any opinions, findings, and conclusions, or recommendations expressed in this material are those of the author(s) and do not necessarily reflect the views of the National Science Foundation.

References

- [1] Besson J, Devillers-Guerville L, Pineau A. Modeling of scatter and size effect in ductile fracture: application to thermal embrittlement of duplex stainless steels. Engineering Fracture Mechanics 2000:22.
- [2] Paredes M, Grolleau V, Wierzbicki T. On ductile fracture of 316L stainless steels at room and cryogenic temperature level: An engineering approach to determine material parameters. Materialia 2020;10:100624. https://doi.org/10.1016/j.mtla.2020.100624.
- [3] Gonzalez-Nino D, Strasser T, Prinz GS. Ultra Low-Cycle Fatigue Behavior Comparison between Additively Manufactured and Rolled 17-4 PH (AISI 630) Stainless Steels. Metals 2021;11:1726. https://doi.org/10.3390/met11111726.
- [4] Pardoen T, Doghri I, Delannay F. Experimental and numerical comparison of void growth models and void coalescence criteria for the prediction of ductile fracture in copper bars. Acta Materialia 1998;46:541–52. https://doi.org/10.1016/S1359-6454(97)00247-4.
- [5] Weck A, Wilkinson DS, Toda H, Maire E. 2D and 3D Visualization of Ductile Fracture. Adv Eng Mater 2006;8:469–72. https://doi.org/10.1002/adem.200600034.
- [6] Giglio M, Manes A, Viganò F. Ductile fracture locus of Ti–6Al–4V titanium alloy. International Journal of Mechanical Sciences 2012;54:121–35. https://doi.org/10.1016/j.ijmecsci.2011.10.003.
- [7] Xu W, Wu H, Ma H, Shan D. Damage evolution and ductile fracture prediction during tube spinning of titanium alloy. International Journal of Mechanical Sciences 2018;135:226–39. https://doi.org/10.1016/j.ijmecsci.2017.11.024.
- [8] Bai Y, Wierzbicki T. Application of extended Mohr–Coulomb criterion to ductile fracture. Int J Fract 2009;161:1. https://doi.org/10.1007/s10704-009-9422-8.
- [9] Papasidero J, Doquet V, Mohr D. Ductile fracture of aluminum 2024-T351 under proportional and non-proportional multi-axial loading: Bao—Wierzbicki results revisited. International Journal of Solids and Structures 2015;69–70:459–74. https://doi.org/10.1016/j.ijsolstr.2015.05.006.
- [10] Wilsdorf HGF. Void initiation, growth, and coalescence in ductile fracture of metals. J Electron Mater 1975;4:791–809. https://doi.org/10.1007/BF02660172.
- [11] Garrison WM, Moody NR. Ductile fracture. Journal of Physics and Chemistry of Solids 1987;48:1035–74. https://doi.org/10.1016/0022-3697(87)90118-1.
- [12] Thomason P. A View on Ductile-Fracture Modelling. Fatigue & Fracture of Engineering Materials & Structures 1998;21:1105–22. https://doi.org/10.1046/j.1460-2695.1998.00077.x.
- [13] Benzerga AA, Leblond J-B. Ductile Fracture by Void Growth to Coalescence. Advances in Applied Mechanics, vol. 44, Elsevier; 2010, p. 169–305. https://doi.org/10.1016/S0065-2156(10)44003-X.
- [14] Tipper CF. The fracture of metals. Metallurgia 1949;39:133–7.
- [15] Goods SH, Brown LM. THE NUCLEATION OF CAVITIES BY PLASTIC DEFORMATION. Perspectives in Creep Fracture, Elsevier; 1983, p. 71–85. https://doi.org/10.1016/B978-0-08-030541-7.50007-2.
- [16] Argon AS, Im J. Separation of second phase particles in spheroidized 1045 steel, Cu-0.6pct Cr alloy, and maraging steel in plastic straining. MTA 1975;6:839–51. https://doi.org/10.1007/BF02672307.
- [17] Beremin FM. Cavity formation from inclusions in ductile fracture of A508 steel. MTA 1981;12:723–31. https://doi.org/10.1007/BF02648336.

- [18] Zhang KS, Bai JB, Fran D. Numerical analysis of the in uence of the Lode parameter on void growth. International Journal of Solids and Structures 2001:10.
- [19] Danas K, Ponte Castañeda P. Influence of the Lode parameter and the stress triaxiality on the failure of elasto-plastic porous materials. International Journal of Solids and Structures 2012;49:1325–42. https://doi.org/10.1016/j.ijsolstr.2012.02.006.
- [20] Kiran R, Khandelwal K. A triaxiality and Lode parameter dependent ductile fracture criterion. Engineering Fracture Mechanics 2014;128:121–38. https://doi.org/10.1016/j.engfracmech.2014.07.010.
- [21] Wen H, Mahmoud H. New Model for Ductile Fracture of Metal Alloys. I: Monotonic Loading. Journal of Engineering Mechanics 2016;142:04015088. https://doi.org/10.1061/(ASCE)EM.1943-7889.0001009.
- [22] Zhu Y, Engelhardt MD. Prediction of ductile fracture for metal alloys using a shear modified void growth model. Engineering Fracture Mechanics 2018;190:491–513. https://doi.org/10.1016/j.engfracmech.2017.12.042.
- [23] Mu L, Zang Y, Wang Y, Li XL, Araujo Stemler PM. Phenomenological uncoupled ductile fracture model considering different void deformation modes for sheet metal forming. International Journal of Mechanical Sciences 2018;141:408–23. https://doi.org/10.1016/j.ijmecsci.2018.04.025.
- [24] Rosenfield AR. Criteria for ductile fracture of two-phase alloys. METALLURGICAL REVIEWS n.d.:12.
- [25] Le Roy G, Embury JD, Edwards G, Ashby MF. A model of ductile fracture based on the nucleation and growth of voids. Acta Metallurgica 1981;29:1509–22. https://doi.org/10.1016/0001-6160(81)90185-1.
- [26] Eshelby JD, Peierls RE. The determination of the elastic field of an ellipsoidal inclusion, and related problems. Proceedings of the Royal Society of London Series A Mathematical and Physical Sciences 1957;241:376–96. https://doi.org/10.1098/rspa.1957.0133.
- [27] Pardoen, Delannay. The Coalescence of Voids in Prestrained Notched Round Copper Bars. Fatigue & Fracture of Engineering Materials & Structures 1998;21:1459–72. https://doi.org/10.1046/j.1460-2695.1998.00123.x.
- [28] Plateau J, Henry G, Crussard C. Quelques nouvelles applications de la microfractographie. Rev Met Paris 1957;54:200–16. https://doi.org/10.1051/metal/195754030200.
- [29] Cox TB, Low JR. An investigation of the plastic fracture of AISI 4340 and 18 Nickel-200 grade maraging steels. Metall Mater Trans B 1974;5:1457–70. https://doi.org/10.1007/BF02646633.
- [30] Floreen S, Hayden HW. Some observations of void growth during the tensile deformation of a high strength steel. Scripta Metallurgica 1970;4:87–94. https://doi.org/10.1016/0036-9748(70)90170-5.
- [31] Psioda JA. The Effect of Microstructure and Strength on the Fracture Toughness of an 18 Ni, 300 Grade Maraging Steel. Carnegie Mellon University, 1977.
- [32] Marino B, Mudry F, Pineau A. Experimental study of cavity growth in ductile rupture. Engineering Fracture Mechanics 1985;22:989–96. https://doi.org/10.1016/0013-7944(85)90038-4.
- [33] Pardoen T, Delannay F. Assessment of void growth models from porosity measurements in cold-drawn copper bars. Metall Mater Trans A 1998;29:1895–909. https://doi.org/10.1007/s11661-998-0014-4.

- [34] Jablokov V, Goto DM, Koss DA. Damage accumulation and failure of HY-100 steel. Metall and Mat Trans A 2001;32:2985–94. https://doi.org/10.1007/s11661-001-0173-z.
- [35] Chae D, Koss DA. Damage accumulation and failure of HSLA-100 steel. Materials Science and Engineering: A 2004;366:299–309. https://doi.org/10.1016/j.msea.2003.08.040.
- [36] Benzerga AA, Besson J, Pineau A. Anisotropic ductile fracture. Acta Materialia 2004;52:4623–38. https://doi.org/10.1016/j.actamat.2004.06.020.
- [37] Maire E, Buffière JY, Salvo L, Blandin JJ, Ludwig W, Létang JM. On the Application of X-ray Microtomography in the Field of Materials Science. Adv Eng Mater 2001;3:539. https://doi.org/10.1002/1527-2648(200108)3:8<539::AID-ADEM539>3.0.CO;2-6.
- [38] Babout L, Maire E, Buffière JY, Fougères R. Characterization by X-ray computed tomography of decohesion, porosity growth and coalescence in model metal matrix composites. Acta Materialia 2001;49:2055–63. https://doi.org/10.1016/S1359-6454(01)00104-5.
- [39] Morgeneyer TF, Starink MJ, Sinclair I. Evolution of voids during ductile crack propagation in an aluminium alloy sheet toughness test studied by synchrotron radiation computed tomography. Acta Materialia 2008;56:1671–9. https://doi.org/10.1016/j.actamat.2007.12.019.
- [40] Babout L, Maire E, Fougères R. Damage initiation in model metallic materials: X-ray tomography and modelling. Acta Materialia 2004;52:2475–87. https://doi.org/10.1016/j.actamat.2004.02.001.
- [41] Maire E, Bordreuil C, Babout L, Boyer J. Damage initiation and growth in metals. Comparison between modelling and tomography experiments. Journal of the Mechanics and Physics of Solids 2005;53:2411–34. https://doi.org/10.1016/j.jmps.2005.06.005.
- [42] Landron C, Maire E, Bouaziz O, Adrien J, Lecarme L, Bareggi A. Validation of void growth models using X-ray microtomography characterization of damage in dual phase steels. Acta Materialia 2011;59:7564–73. https://doi.org/10.1016/j.actamat.2011.08.046.
- [43] Hsiao CN, Chiou CS, Yang JR. Aging reactions in a 17-4 PH stainless steel. Materials Chemistry and Physics 2002;74:134–42. https://doi.org/10.1016/S0254-0584(01)00460-6.
- [44] Bjorhovde R. Development and use of high performance steel. Journal of Constructional Steel Research 2004;60:393–400. https://doi.org/10.1016/S0143-974X(03)00118-4.
- [45] Sajid HU, Kiran R. Influence of high stress triaxiality on mechanical strength of ASTM A36, ASTM A572 and ASTM A992 steels. Construction and Building Materials 2018;176:129–34. https://doi.org/10.1016/j.conbuildmat.2018.05.018.
- [46] Hu G, Morovat MA, Lee J, Schell E, Engelhardt M. Elevated Temperature Properties of ASTM A992 Steel. Structures Congress 2009, Austin, Texas, United States: American Society of Civil Engineers; 2009, p. 1–10. https://doi.org/10.1061/41031(341)118.
- [47] Stoudt MR, Ricker RE, Lass EA, Levine LE. Influence of Postbuild Microstructure on the Electrochemical Behavior of Additively Manufactured 17-4 PH Stainless Steel. JOM 2017;69:506–15. https://doi.org/10.1007/s11837-016-2237-y.
- [48] AlMangour B, Yang J-M. Improving the surface quality and mechanical properties by shot-peening of 17-4 stainless steel fabricated by additive manufacturing. Materials & Design 2016;110:914–24. https://doi.org/10.1016/j.matdes.2016.08.037.
- [49] Sajid HU, Naik DL, Kiran R. Microstructure—Mechanical Property Relationships for Post-Fire Structural Steels. Journal of Materials in Civil Engineering 2020;32:04020133. https://doi.org/10.1061/(ASCE)MT.1943-5533.0003190.

- [50] Kiran R, Khandelwal K. Experimental Studies and Models for Ductile Fracture in ASTM A992 Steels at High Triaxiality. Journal of Structural Engineering 2014;140:04013044. https://doi.org/10.1061/(ASCE)ST.1943-541X.0000828.
- [51] Kiran R, Khandelwal K. A micromechanical model for ductile fracture prediction in ASTM A992 steels. Engineering Fracture Mechanics 2013;102:101–17. https://doi.org/10.1016/j.engfracmech.2013.02.021.
- [52] Leksycki K, Królczyk JB. Comparative assessment of the surface topography for different optical profilometry techniques after dry turning of Ti6Al4V titanium alloy. Measurement 2021;169:108378. https://doi.org/10.1016/j.measurement.2020.108378.
- [53] Struzikiewicz G, Sioma A. Evaluation of Surface Roughness and Defect Formation after The Machining of Sintered Aluminum Alloy AlSi10Mg. Materials 2020;13:1662. https://doi.org/10.3390/ma13071662.
- [54] Hirose R, Miyazaki H, Bandou R, Watanabe N, Yoshida T, Daidoji T, et al. Stability of SARS-CoV-2 and influenza virus varies across different paper types. Journal of Infection and Chemotherapy 2022;28:252–6. https://doi.org/10.1016/j.jiac.2021.11.006.
- [55] Kiss P, Jonkers L, Hudáčková N, Reuter RT, Donner B, Fischer G, et al. Determinants of Planktonic Foraminifera Calcite Flux: Implications for the Prediction of Intra- and Inter-Annual Pelagic Carbonate Budgets. Global Biogeochemical Cycles 2021;35:e2020GB006748. https://doi.org/10.1029/2020GB006748.
- [56] Felix K, Tobias S, Jan H, Nicolas S, Michael M. Measurements of transepithelial electrical resistance (TEER) are affected by junctional length in immature epithelial monolayers. Histochem Cell Biol 2021;156:609–16. https://doi.org/10.1007/s00418-021-02026-4.
- [57] Bond AD, Edgecombe GD. Phylogenetic response of naraoiid arthropods to early–middle Cambrian environmental change. Palaeontology 2021;64:161–77. https://doi.org/10.1111/pala.12516.
- [58] Gyarmati J, Maróti B, Kasztovszky Z, Döncző B, Szikszai Z, Aradi LE, et al. Hidden behind the mask: An authentication study on the Aztec mask of the Museum of Ethnography, Budapest, Hungary. Forensic Science International 2022;333:111236. https://doi.org/10.1016/j.forsciint.2022.111236.
- [59] Youssef G. Chapter 11 Characterization of polymers. In: Youssef G, editor. Applied Mechanics of Polymers, Elsevier; 2022, p. 273–99. https://doi.org/10.1016/B978-0-12-821078-9.00016-8.
- [60] Schneider CA, Rasband WS, Eliceiri KW. NIH Image to ImageJ: 25 years of image analysis. Nat Methods 2012;9:671–5. https://doi.org/10.1038/nmeth.2089.
- [61] Dassault Systemes. ABAQUS/standard analysis user's manual 2019.
- [62] Gurson AL. Continuum Theory of Ductile Rupture by Void Nucleation and Growth: Part I—Yield Criteria and Flow Rules for Porous Ductile Media. Journal of Engineering Materials and Technology 1977;99:2–15. https://doi.org/10.1115/1.3443401.
- [63] Tvergaard V. On localization in ductile materials containing spherical voids. Int J Fract 1982;18:237–52. https://doi.org/10.1007/BF00015686.
- [64] Tvergaard V, Needleman A. Analysis of the cup-cone fracture in a round tensile bar. Acta Metallurgica 1984;32:157–69. https://doi.org/10.1016/0001-6160(84)90213-X.
- [65] Gologanu M, Leblond J-B, Devaux J. Approximate models for ductile metals containing non-spherical voids—Case of axisymmetric prolate ellipsoidal cavities. Journal of the Mechanics and Physics of Solids 1993;41:1723–54. https://doi.org/10.1016/0022-5096(93)90029-F.

- [66] Gologanu M, Leblond J-B, Devaux J. Approximate Models for Ductile Metals Containing Nonspherical Voids—Case of Axisymmetric Oblate Ellipsoidal Cavities. Journal of Engineering Materials and Technology 1994;116:290–7. https://doi.org/10.1115/1.2904290.
- [67] Benzerga AA, Besson J. Plastic potentials for anisotropic porous solids. European Journal of Mechanics A/Solids 2001;20:397–434. https://doi.org/10.1016/S0997-7538(01)01147-0.
- [68] Rice JR, Tracey DM. On the ductile enlargement of voids in triaxial stress fields*. Journal of the Mechanics and Physics of Solids 1969;17:201–17. https://doi.org/10.1016/0022-5096(69)90033-7.
- [69] d'Escatha Y, Devaux J. Numerical Study of Initiation, Stable Crack Growth, and Maximum Load, with a Ductile Fracture Criterion Based on the Growth of Holes. In: Landes J, Begley J, Clarke G, editors. Elastic-Plastic Fracture, 100 Barr Harbor Drive, PO Box C700, West Conshohocken, PA 19428-2959: ASTM International; 1979, p. 229-229–20. https://doi.org/10.1520/STP35833S.
- [70] Hancock JW, Mackenzie AC. On the mechanisms of ductile failure in high-strength steels subjected to multi-axial stress-states. Journal of the Mechanics and Physics of Solids 1976;24:147–60. https://doi.org/10.1016/0022-5096(76)90024-7.
- [71] Kanvinde AM, Deierlein GG. The Void Growth Model and the Stress Modified Critical Strain Model to Predict Ductile Fracture in Structural Steels. Journal of Structural Engineering 2006;132:1907–18. https://doi.org/10.1061/(ASCE)0733-9445(2006)132:12(1907).
- [72] Jia L-J, Kuwamura H. Ductile Fracture Simulation of Structural Steels under Monotonic Tension. Journal of Structural Engineering 2014;140:04013115. https://doi.org/10.1061/(ASCE)ST.1943-541X.0000944.
- [73] Bates D, Watts D. Nonlinear Regression Analysis and Its Applications. John Wiley & Sons, Inc.; 1988.

Table 1: Chemical composition of 17-4 PH stainless steel and ASTM A992 steel

Chemical	17-4 PH	ASTM
Composition (%)	1/-4 РП	A992
Carbon (C)	0.0700	0.1500
Manganese (Mn)	1.0000	0.6900
Phosphorous (P)	0.0400	0.0180
Sulphur (S)	0.0300	0.0040
Silicon (Si)	1.0000	0.1800
Copper (Cu)	5.0000	0.2400
Chromium (Cr)	15-17.5	0.1500
Nickel (Ni)	3-5	0.0880
Molybdenum (Mo)	-	0.0195
Vanadium (V)	-	0.0048
Titanium (Ti)	-	0.0012
Nobium (Nb)	0.1500	0.0024
Iron (Fe)	Balance	Balance

Table 2: Dimensions of uniaxial tensile test specimens made of 17-4 PH stainless steel and ASTM A992 steel

		Radius	Depth	Diameter
Notch	Material	(R)	(D)	(d)
		(mm)	(mm)	(mm)
CN1	17-4 PH	0.5	-	5
CN2	17-4 PH	1	-	5
CN2	ASTM A992	1	-	10
CN3	17-4 PH	1.5	-	5
CN4	ASTM A992	2	-	10
CN5	ASTM A992	3	-	10
UN	ASTM A992	1	1	10
RU	17-4 PH	-	-	5
RU	ASTM A992	-	-	10

Table 3: Skewness and Kurtosis measures for the 17-4 PH stainless steel void size distributions

Specimen Name	Zone	Skewness	Kurtosis
	Zone 1	0.78	0.09
CN1	Zone 2	0.395	-0.522
	Zone 3	0.375	-0.13
	Zone 1	0.385	-0.531
CN2	Zone 2	0.55	0.046
	Zone 3	0.365	-0.057
CN3	Zone 1	0.646	0.835
	Zone 2	0.428	0.006
	Zone 3	0.373	-0.486
RU	Zone 1	0.526	0.464
	Zone 2	0.483	-0.288
	Zone 3	0.481	-0.561

Table 4: Skewness and Kurtosis measures for the ASTM A992 steel void size distributions

Specimen Name	Zone	Skewness	Kurtosis
	Zone 1	0.179	-0.461
CN2	Zone 2	0.227	-0.417
	Zone 3	0.227	-0.796
	Zone 1	0.032	-0.152
CN4	Zone 2	0.299	-0.296
	Zone 3	0.265	0.145
	Zone 1	0.234	-0.352
CN5	Zone 2	0.445	-0.29
	Zone 3	0.323	-0.218
	Zone 1	0.365	-0.417
RU	Zone 2	0.595	0.059
	Zone 3	0.293	-0.092
UN	Zone 1	0.276	-0.179
	Zone 2	-0.361	-0.334
	Zone 3	0.373	-0.488

Table 5: Fracture model parameters and characteristic length of 17-4 PH stainless steel and ASTM A992 steel

Material	Model Parameters			Characteristic Length
	$ln(R_0)$	α	β	(μm)
17-4 PH	0.508	0.0684	2.15	50
ASTM A992	0.69	0.0175	2.3	75

Table 6: Comparison of experimental and predicted fracture displacement for 17-4 PH stainless steel and ASTM A992 steel test specimens

Material	Specimen -	Δ_{exp}	Δ_{Pre}	Diff
	Specifici	(mm)	(mm)	(%)
17-4 PH	RU	2.69	2.3	11.1
	CN1	1.28	1.28	0.0
	CN2	0.8	0.72	10.0
	CN3	0.47	0.45	4.4
_	RU	11.88	11.5	3.2
ASTM A992	CN2	4.54	4.54	0.0
	CN4	2.7	2.5	7.4
	CN5	2.2	1.9	13.6
	UN	2.72	2.54	6.6

Figures

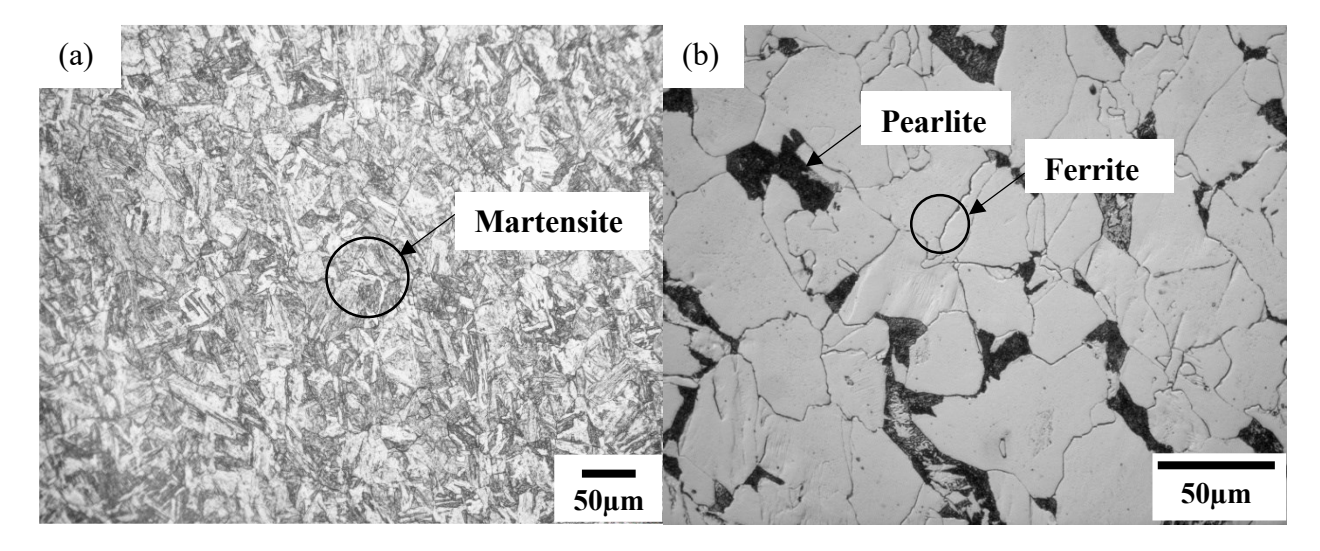


Figure 1: (a) Martensitic microstructure of 17-4 PH stainless steel and (b) ferrite-pearlite microstructure of ASTM A992 structural steel

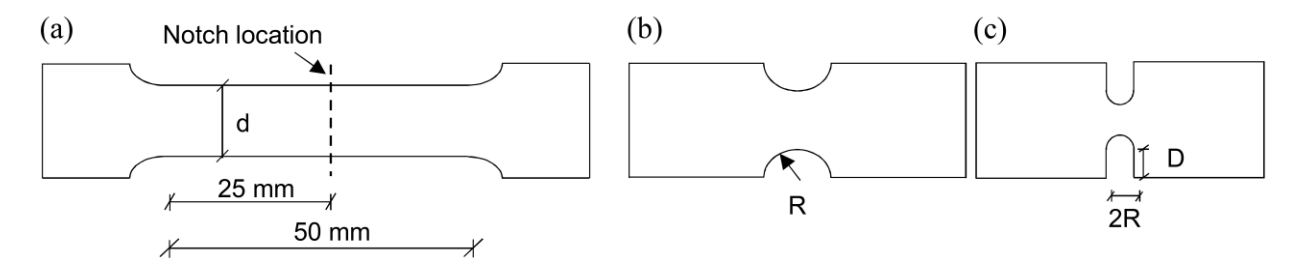


Figure 2: Geometry of (a) axisymmetric tensile steel specimen; (b) C-notch; and (c) U-notch

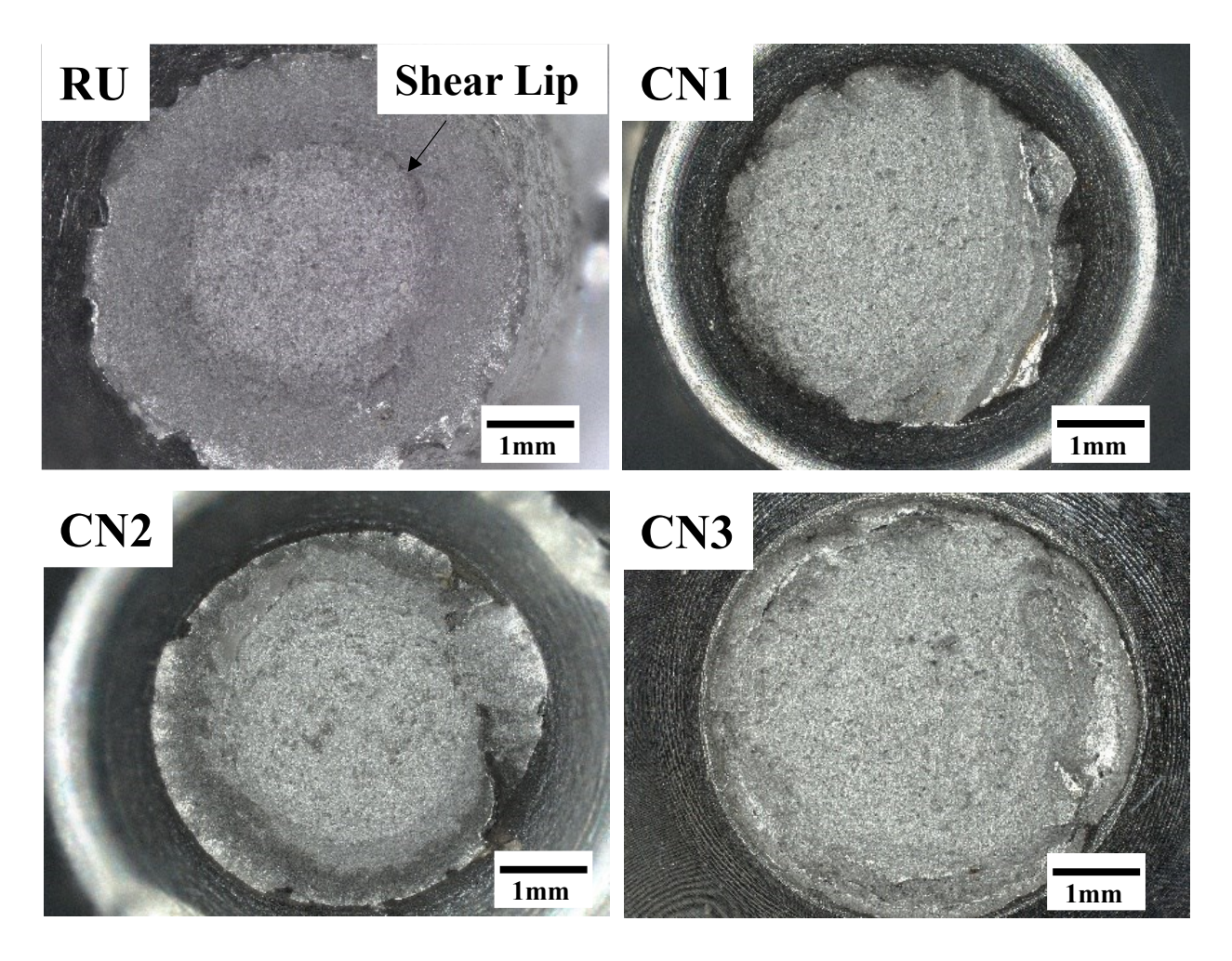


Figure 3: Macroscopic fracture surfaces of 17-4 PH stainless steel test specimens (RU- reference unnotched; CN1, CN2, and CN3: C-notch with notch radii of 0.5 mm, 1.0 mm, and 1.5 mm, respectively). Shear lip is observed in the unnotched specimen only.

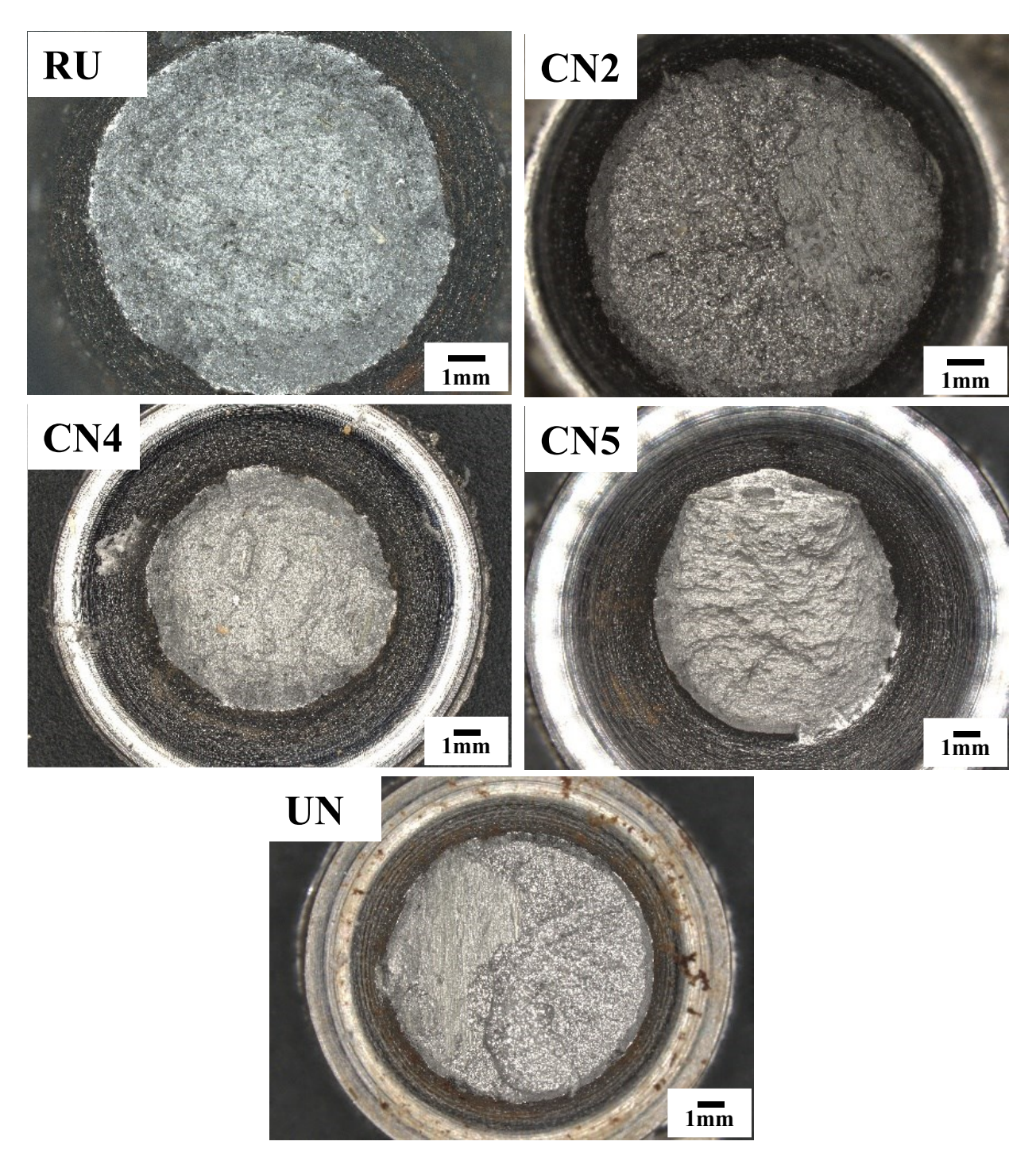


Figure 4: Macroscopic fracture surfaces of ASTM A992 structural steel test specimens (RU: reference unnotched; CN2, CN4, and CN5: C-notch with notch radii of 1.0 mm, 2.0 mm, and 3.0 mm, respectively; UN: U-notch with notch radius 1.0 mm and depth 1.0 mm)

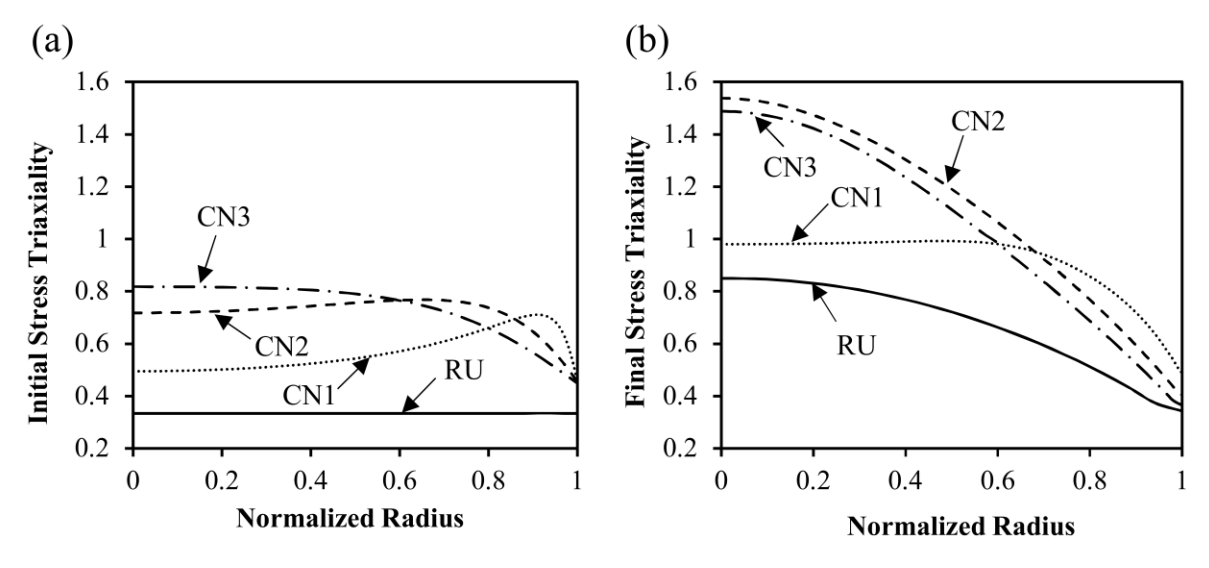


Figure 5: (a) Initial and (b) final stress triaxiality profiles of 17-4PH stainless steel specimens

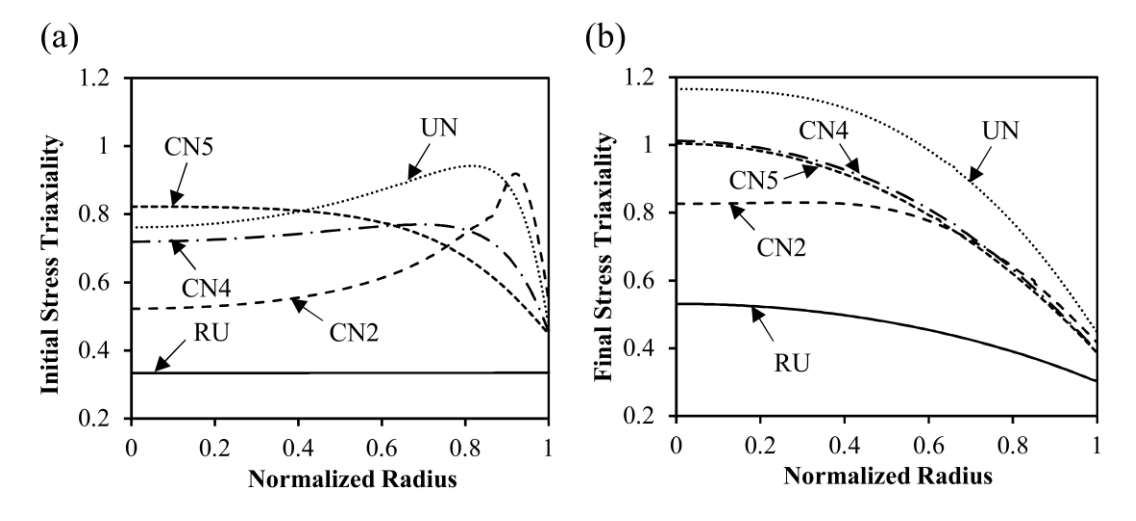


Figure 6: (a) Initial and (b) final stress triaxiality profiles of ASTM A992 steel specimens

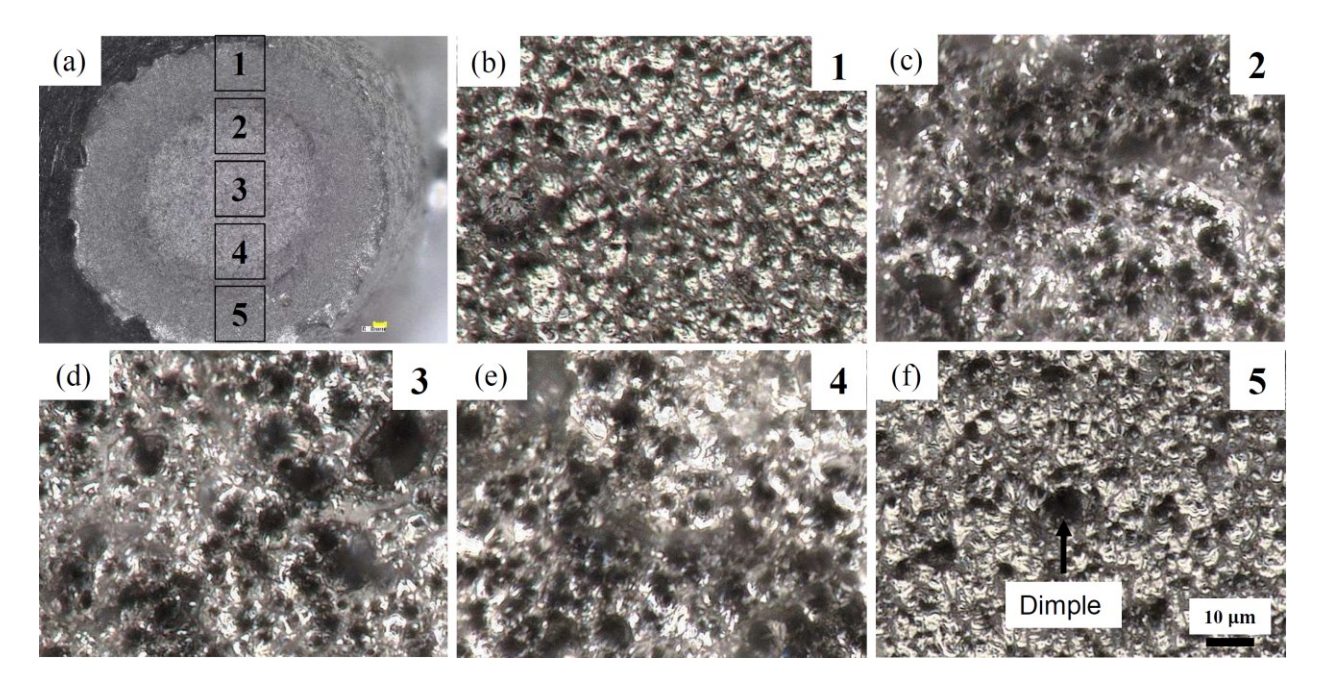


Figure 7: (a) Macroscopic fracture surface image and (b)-(f) micro-scale fracture images of 17-4 PH stainless steel reference unnotched specimen (RU) in regions 1, 2, 3, 4, and 5

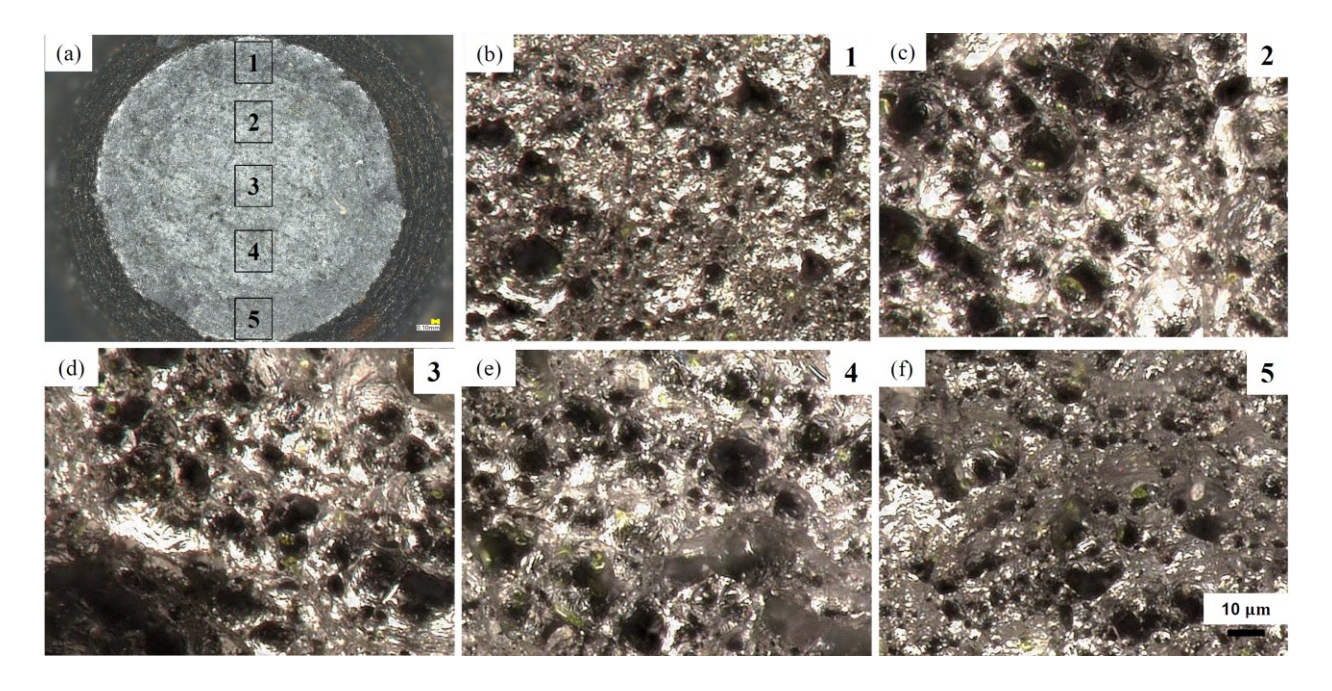


Figure 8: (a) Macroscopic fracture surface image and (b)-(f) micro-scale fracture images of ASTM A992 structural steel reference unnotched specimen (RU) in regions 1, 2, 3, 4, and 5

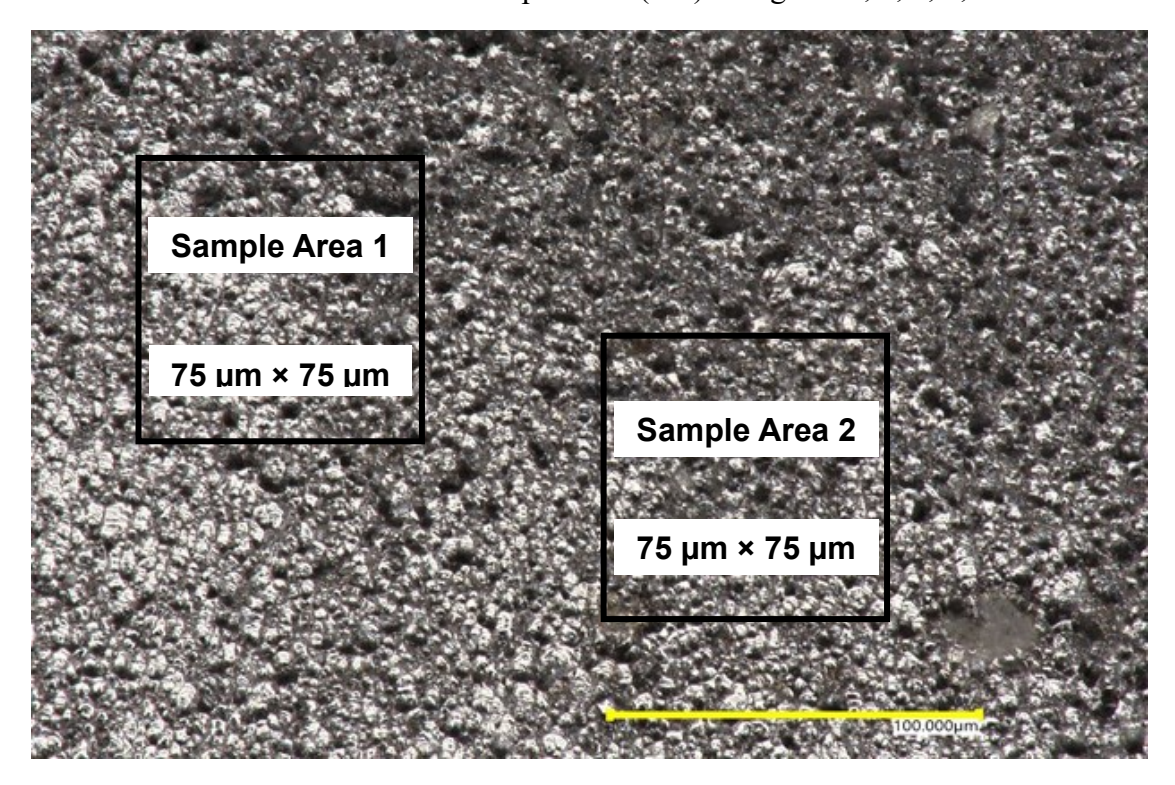


Figure 9: Sample regions for extracting microvoid cross-section areas on the surface of a fractured test specimen

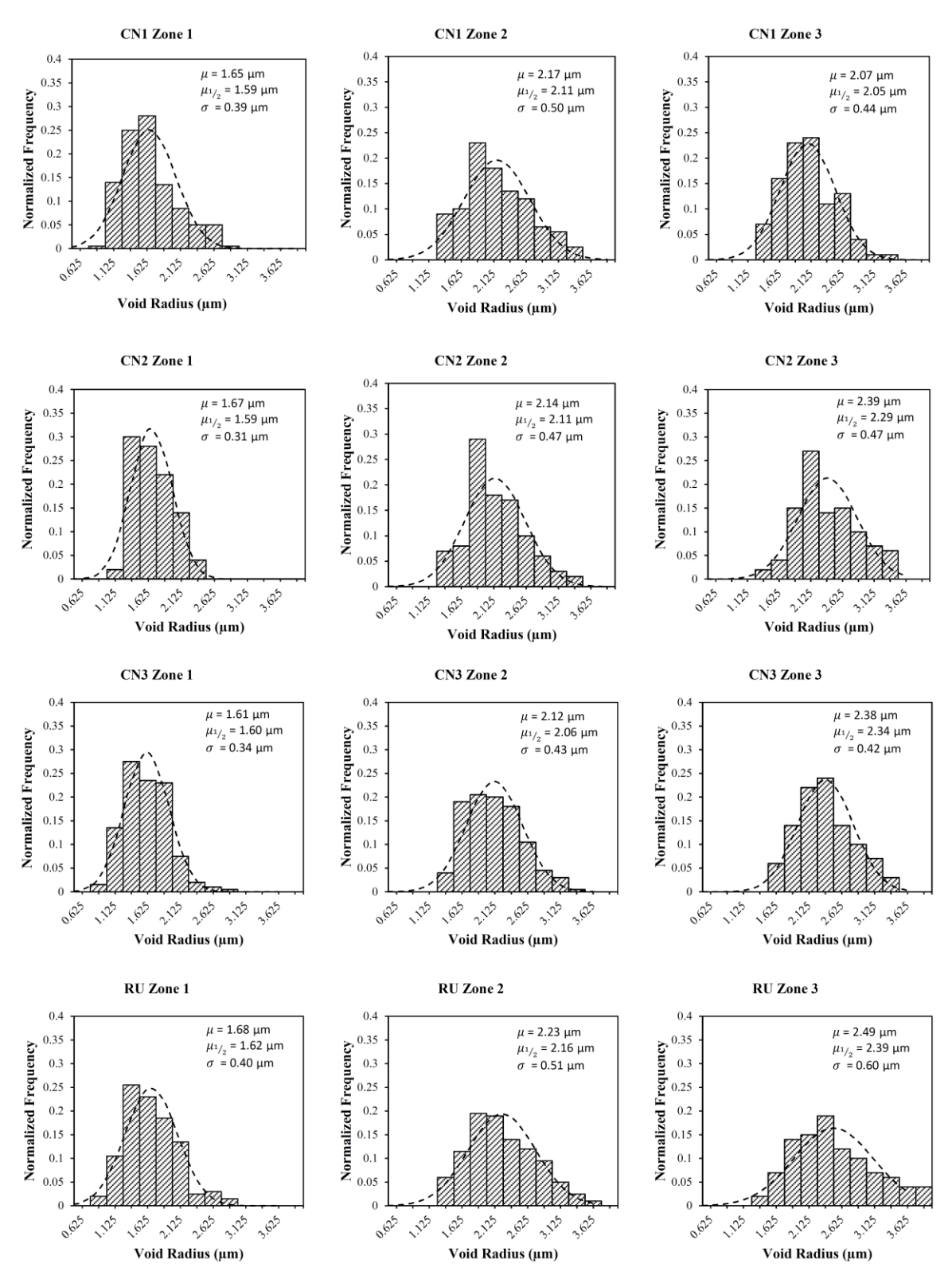


Figure 10: Histograms of void size distributions (equivalent void radius) for 17-4 PH stainless steel fracture specimens in all three zones

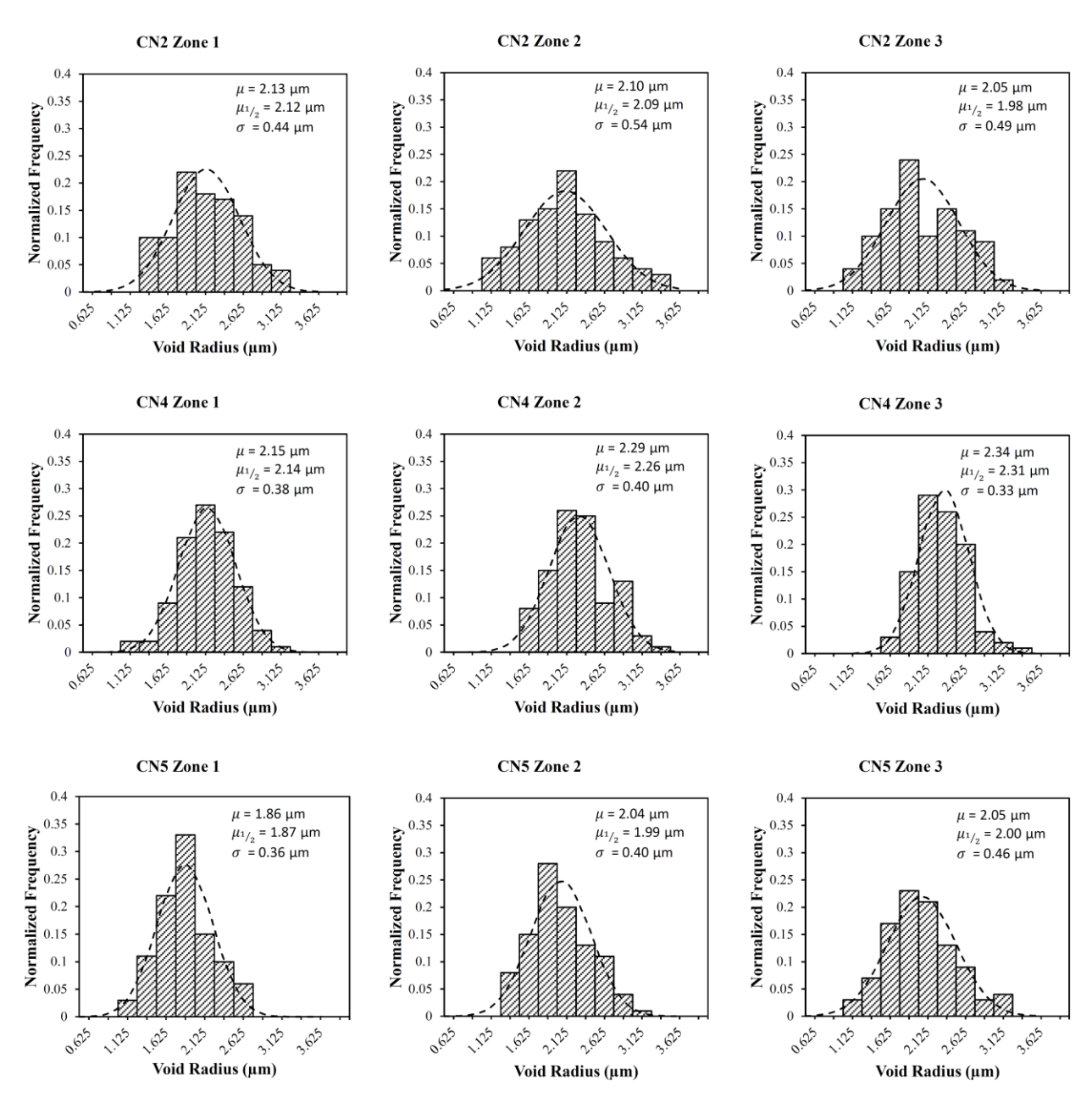


Figure 11: Histograms of void size distributions (equivalent void radius) for ASTM A992 steel C-notch fracture specimens in all three zones

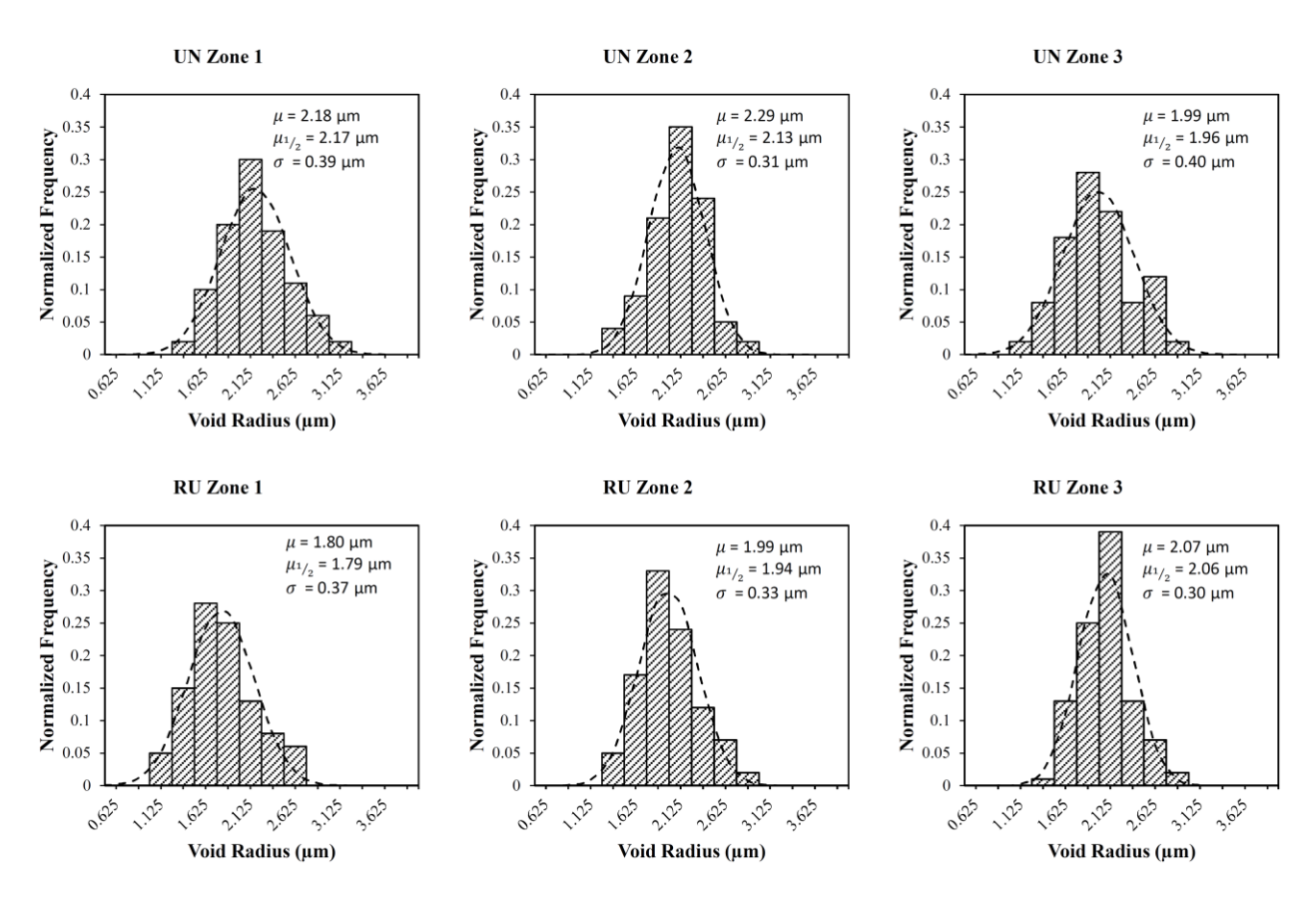


Figure 12: Histograms of void size distributions (equivalent void radius) for ASTM A992 steel Unotch (UN) and reference unnotched (RU) fracture specimens in all three zones

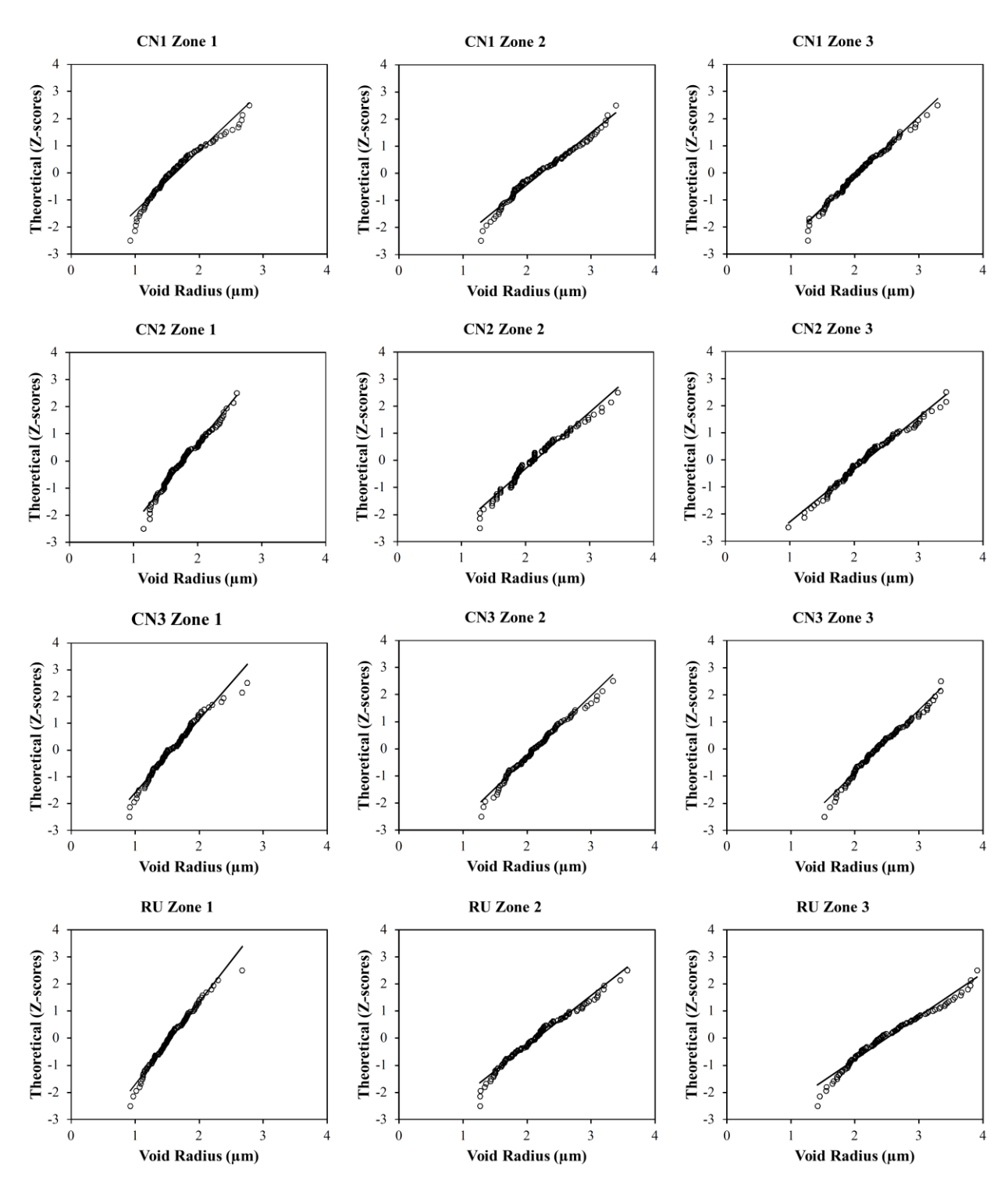


Figure 13: Normal probability plots of void size (equivalent void radius) for 17-4 PH steel fracture specimens

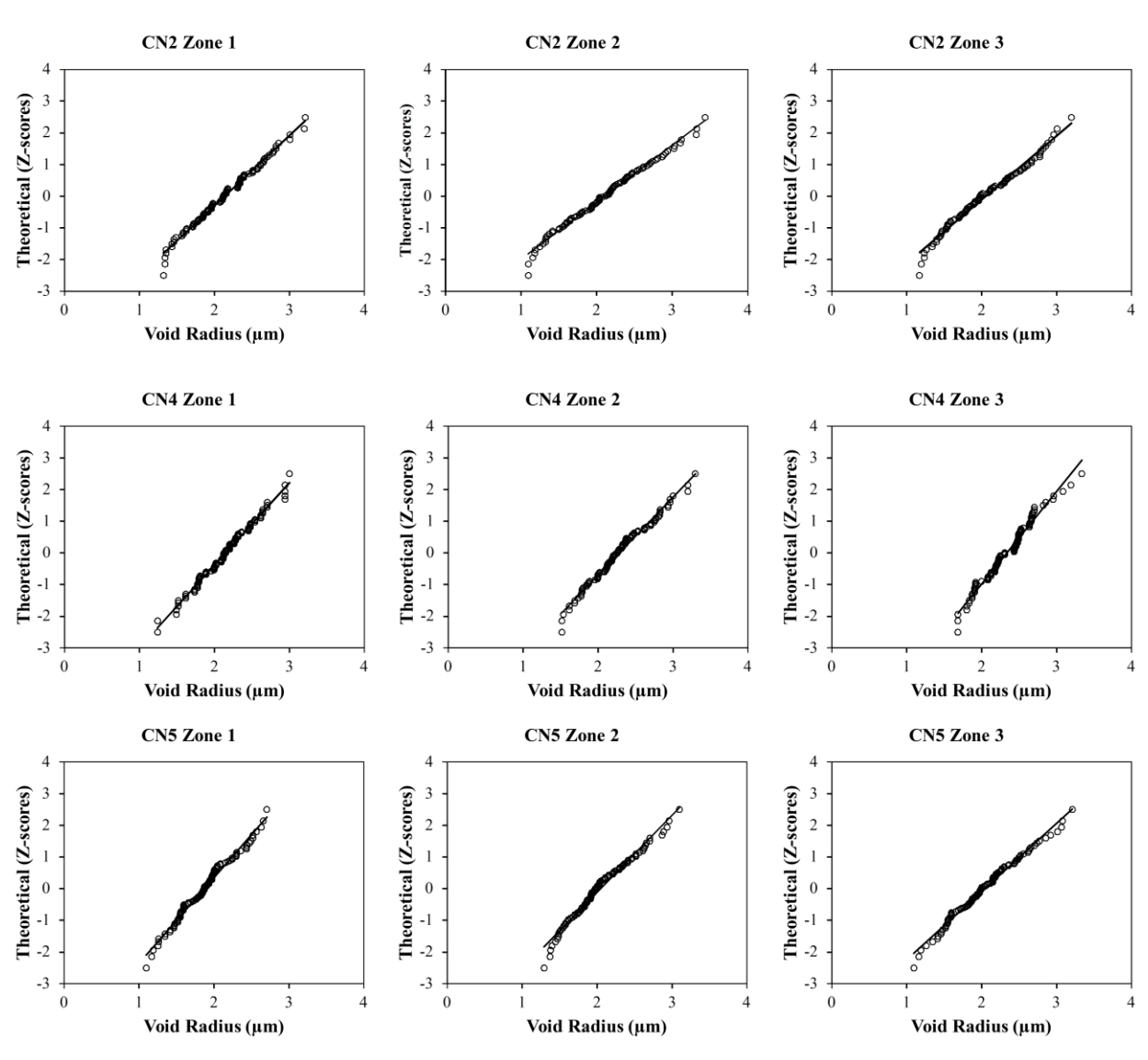


Figure 14: Normal probability plots of void size (equivalent void radius) for ASTM A992 steel C-notch fracture specimens

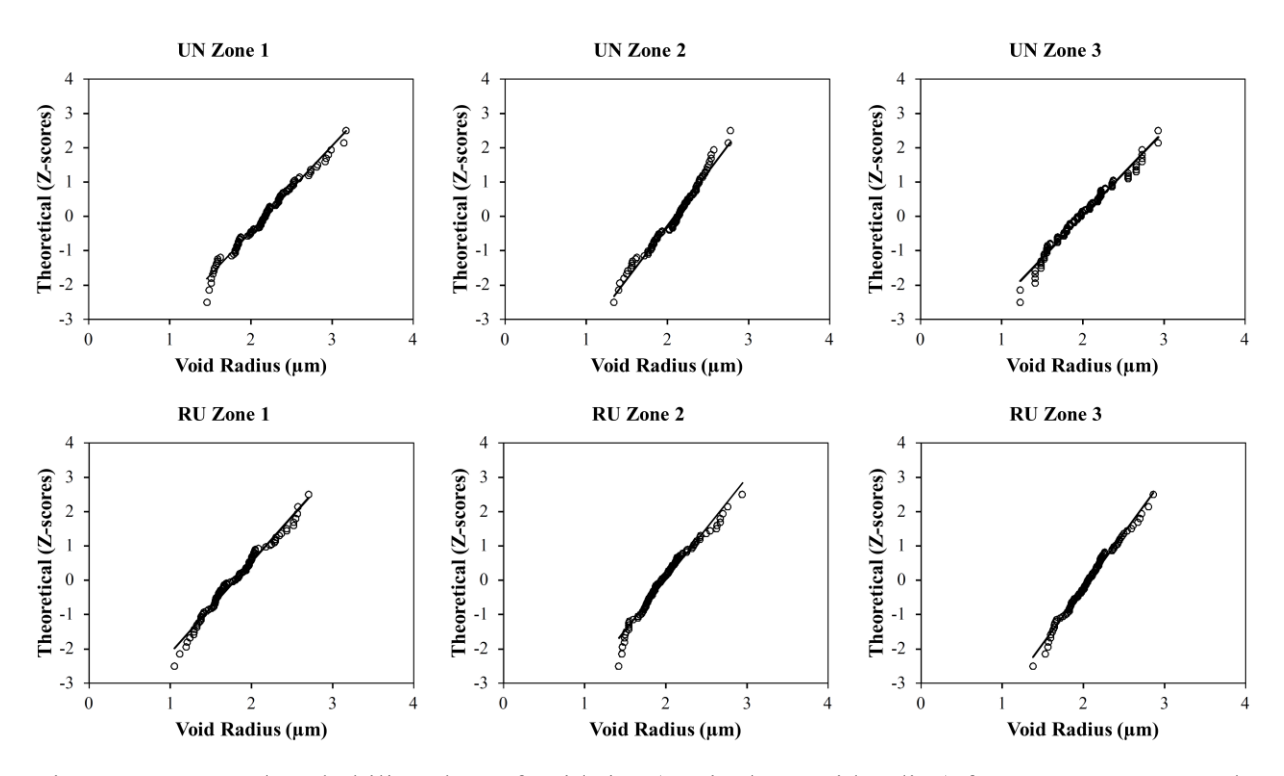


Figure 15: Normal probability plots of void size (equivalent void radius) for ASTM A992 steel Unotch (UN) and reference unnotched (RU) fracture specimens

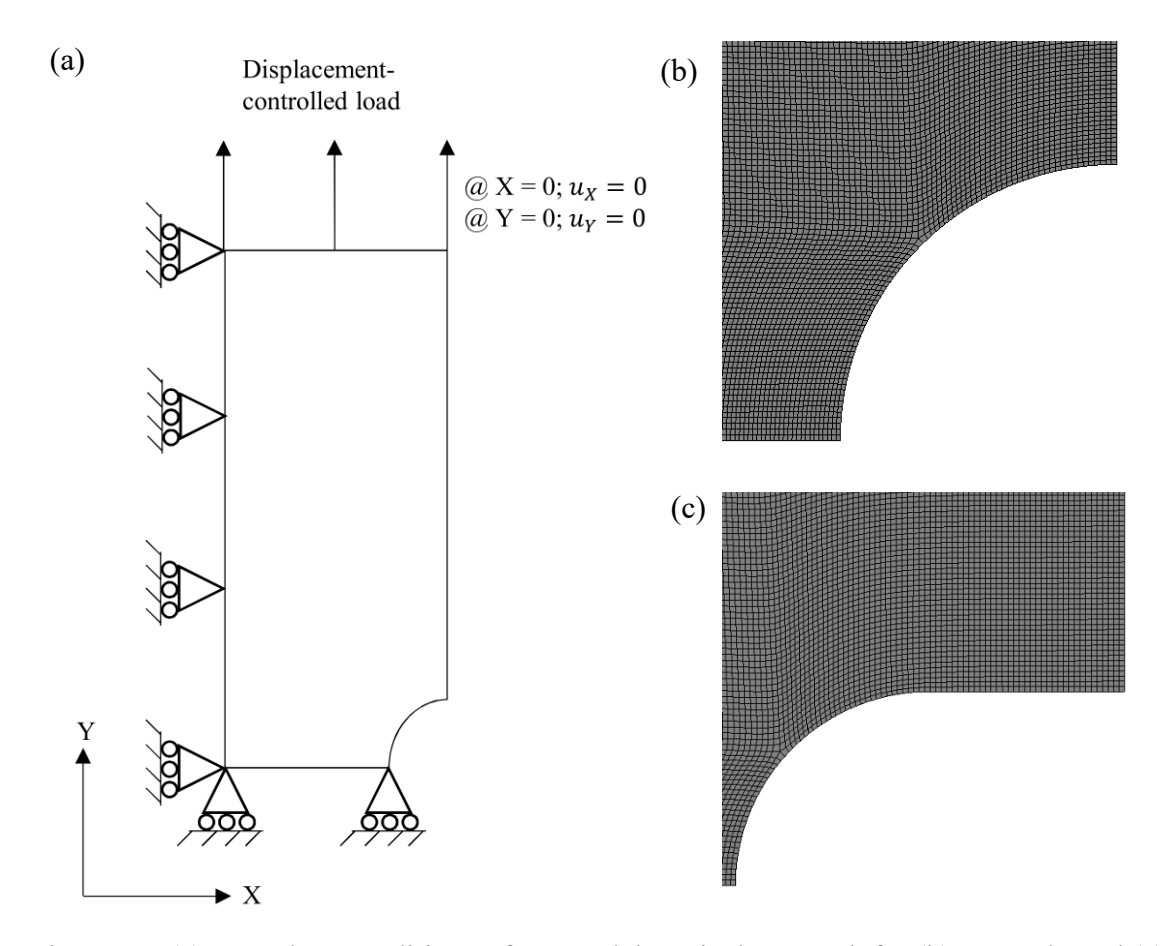


Figure 16: (a) Boundary conditions of FE model; typical FE mesh for (b) C-notch, and (c) U-notch

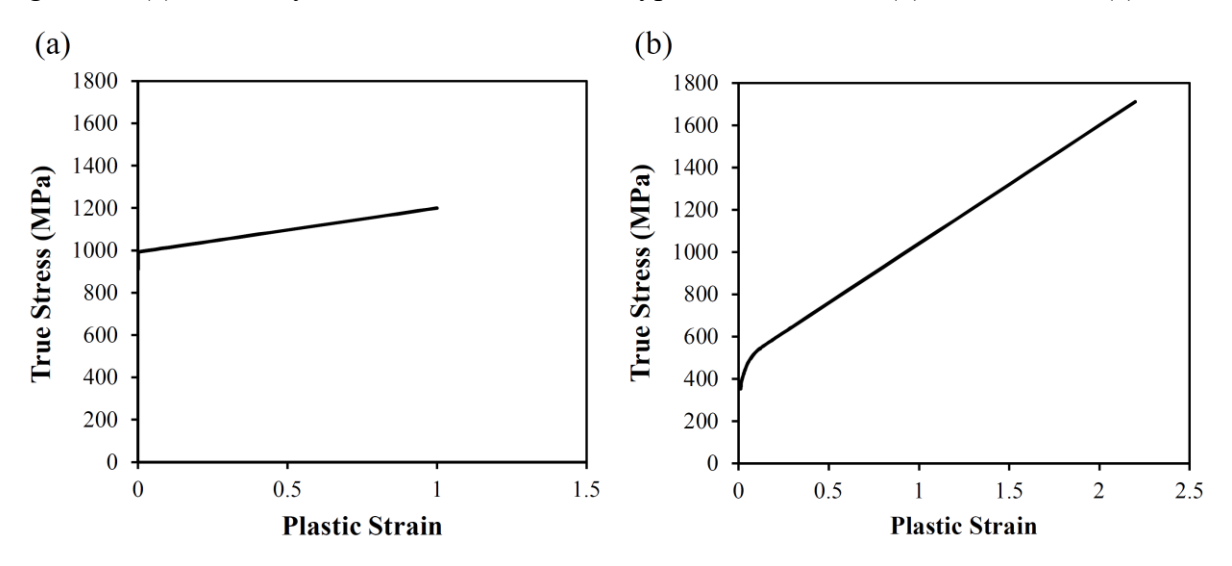


Figure 17: Strain hardening curves for (a) 17-4 PH stainless steel and (b) ASTM A992 structural steel

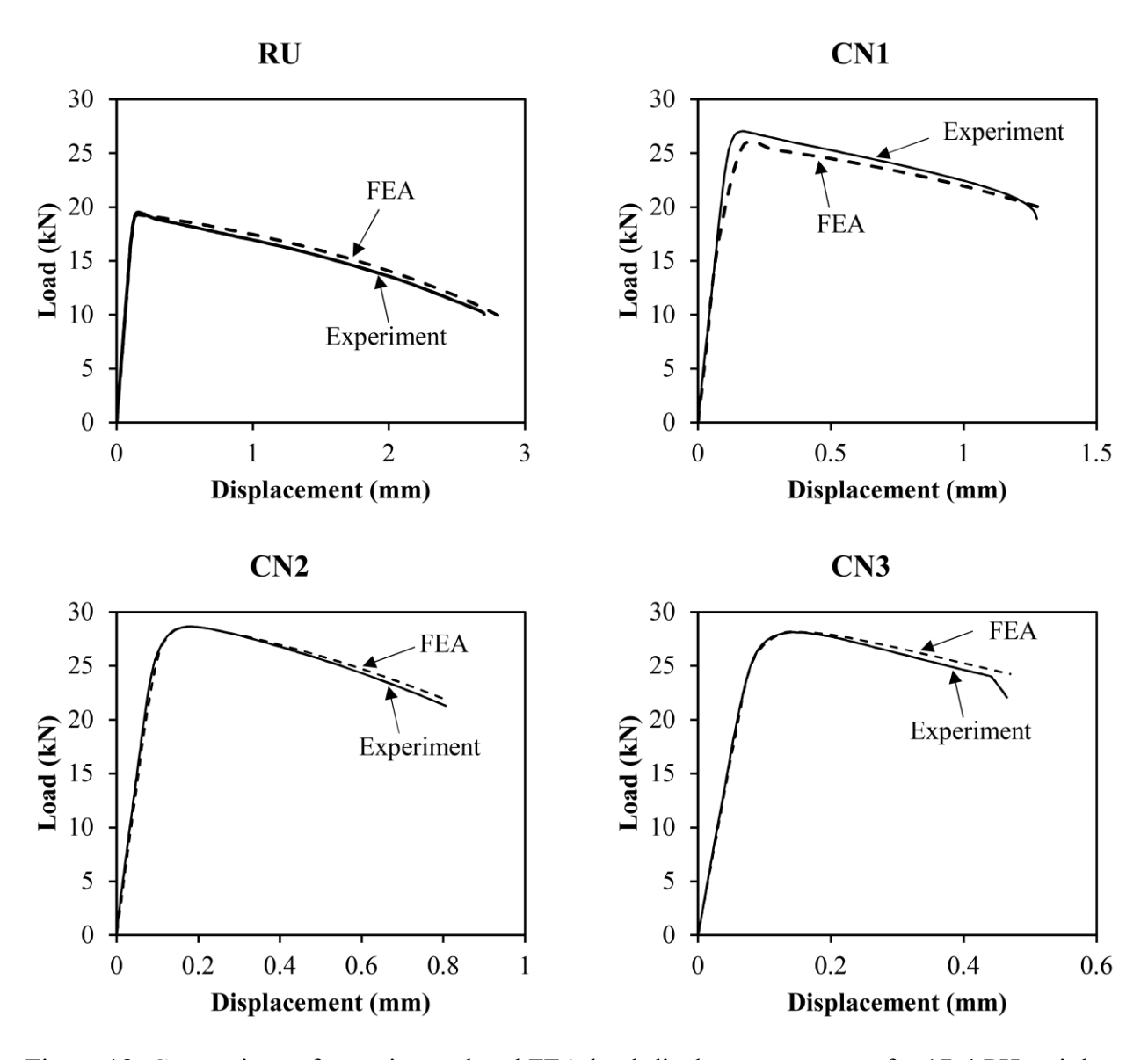


Figure 18: Comparison of experimental and FEA load-displacement curves for 17-4 PH stainless steel fracture specimens

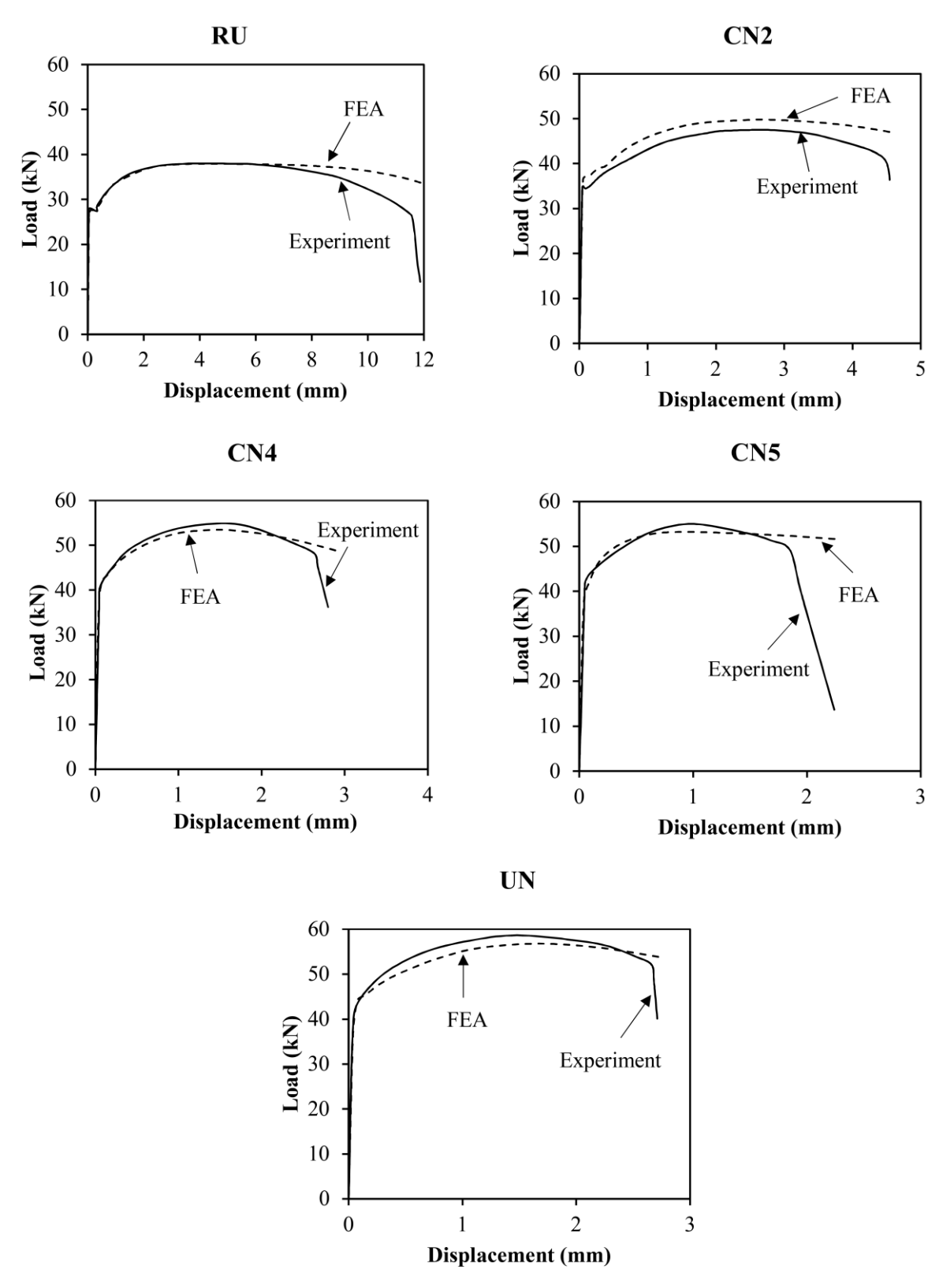


Figure 19: Comparison of experimental and FEA load-displacement curves for ASTM A992 steel fracture specimens

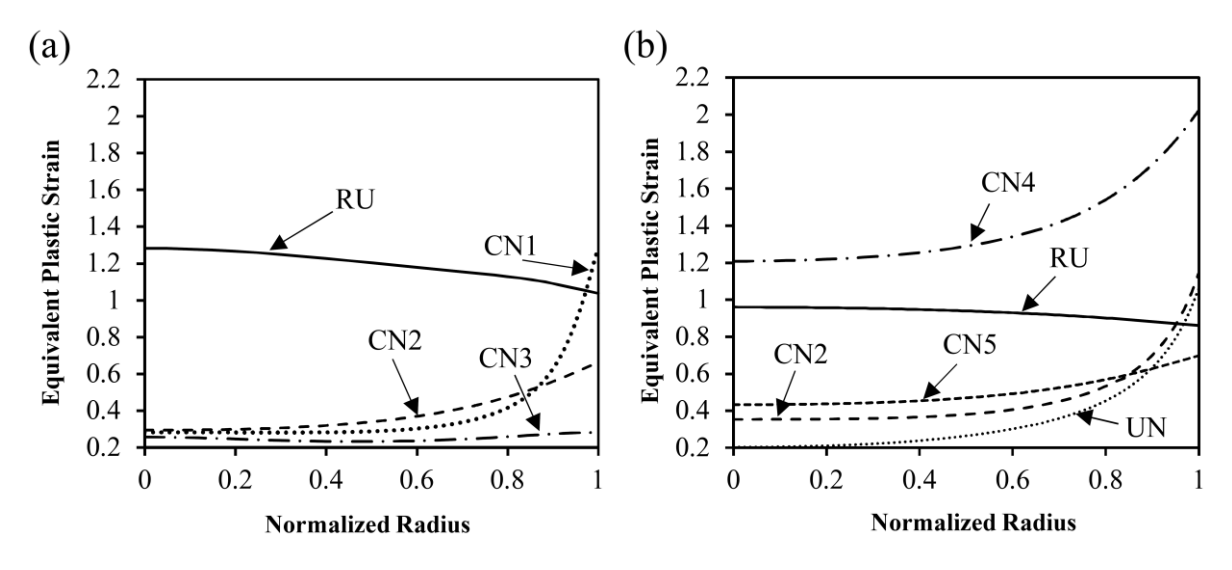


Figure 20: Equivalent plastic strain profiles at failure for (a) 17-4 PH steel and (b) ASTM A992 steel

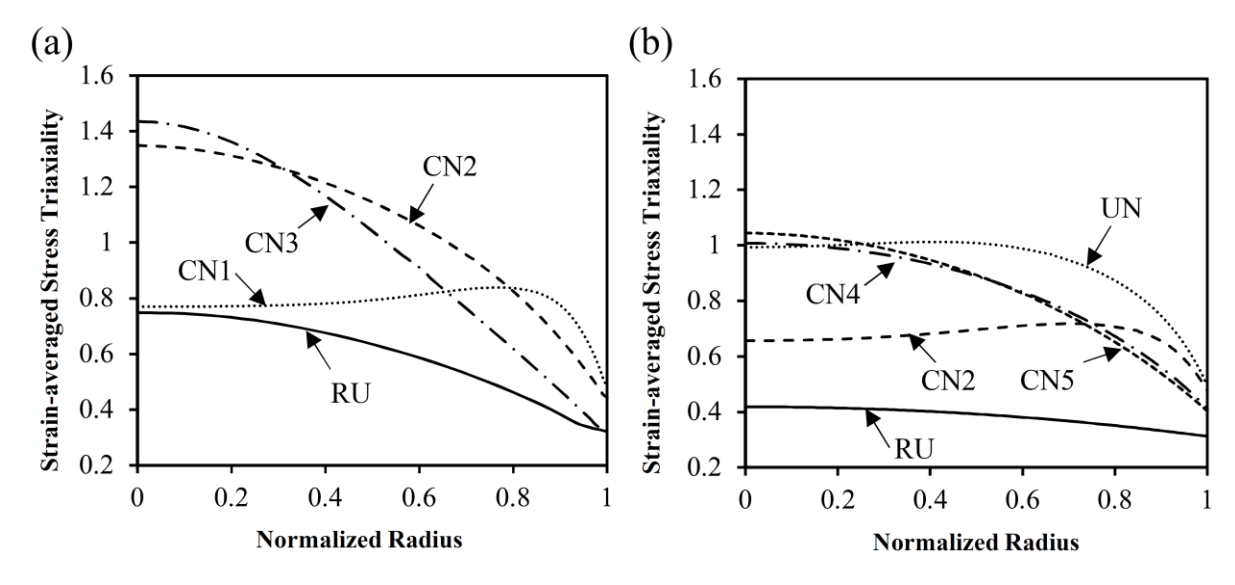


Figure 21: Strain-averaged stress triaxiality profiles for (a) 17-4 PH steel and (b) ASTM A992 steel

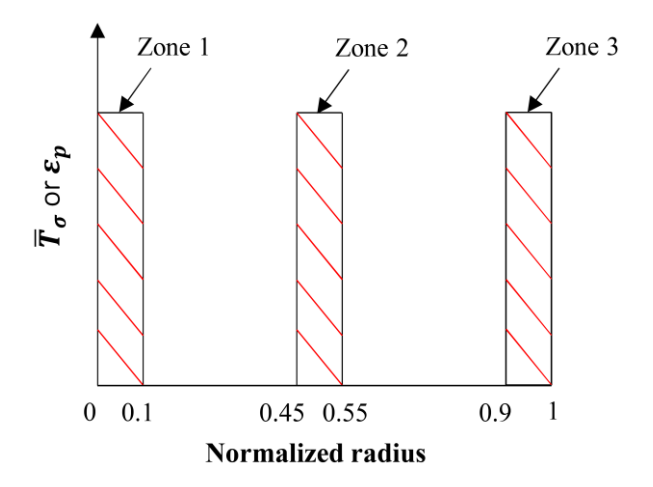


Figure 22: Span of distinct fracture zones on the surface of a fractured steel specimen

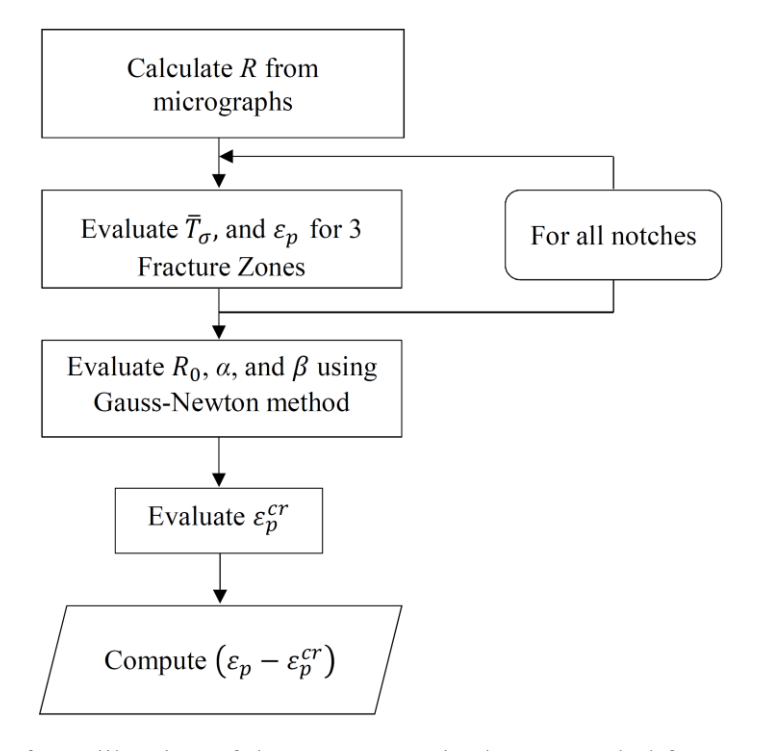


Figure 23: Flowchart for calibration of the parameters in the uncoupled fracture criterion

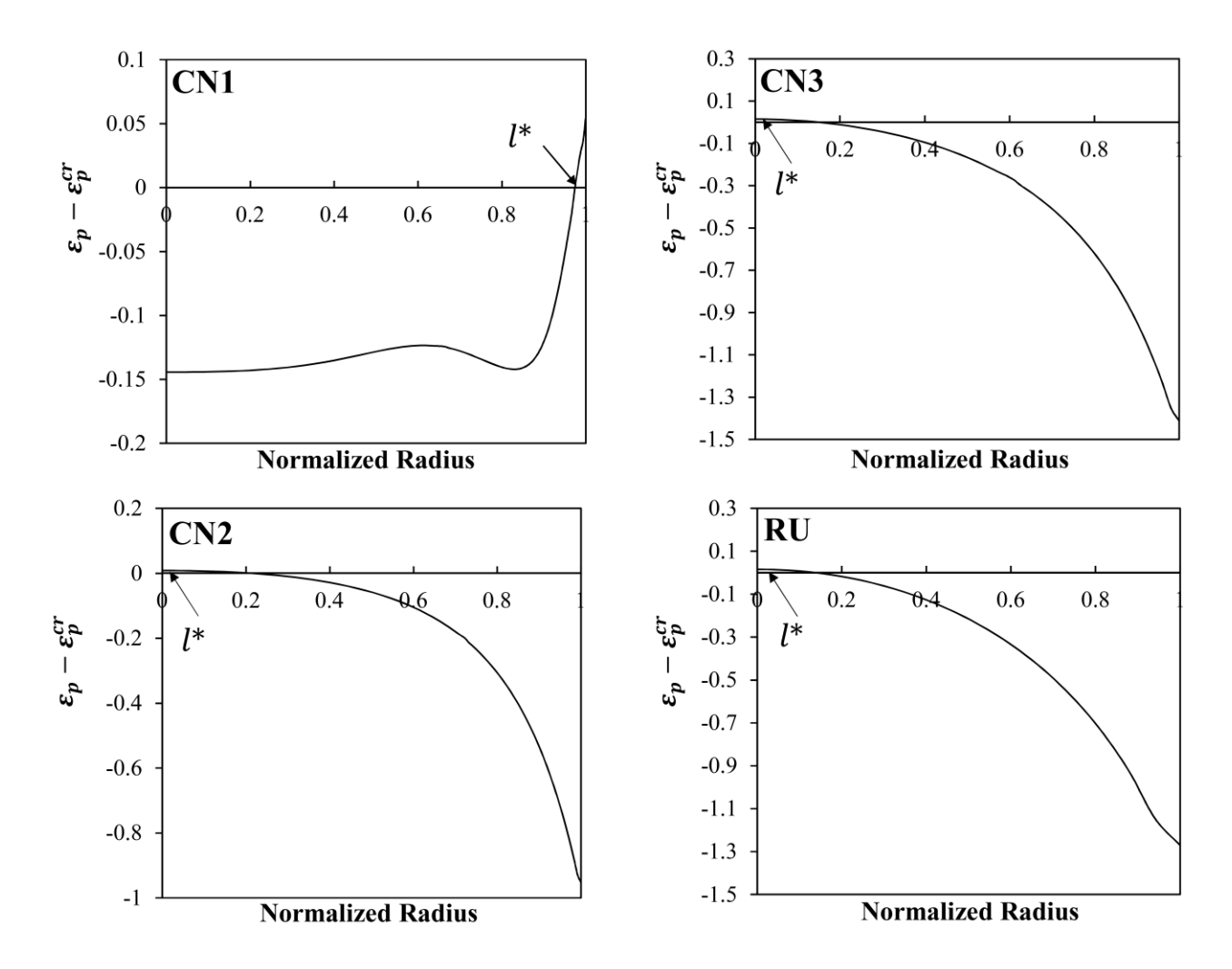


Figure 24: $(\varepsilon_p - \varepsilon_p^{cr})$ profiles of 17-4 PH stainless steel fracture specimens

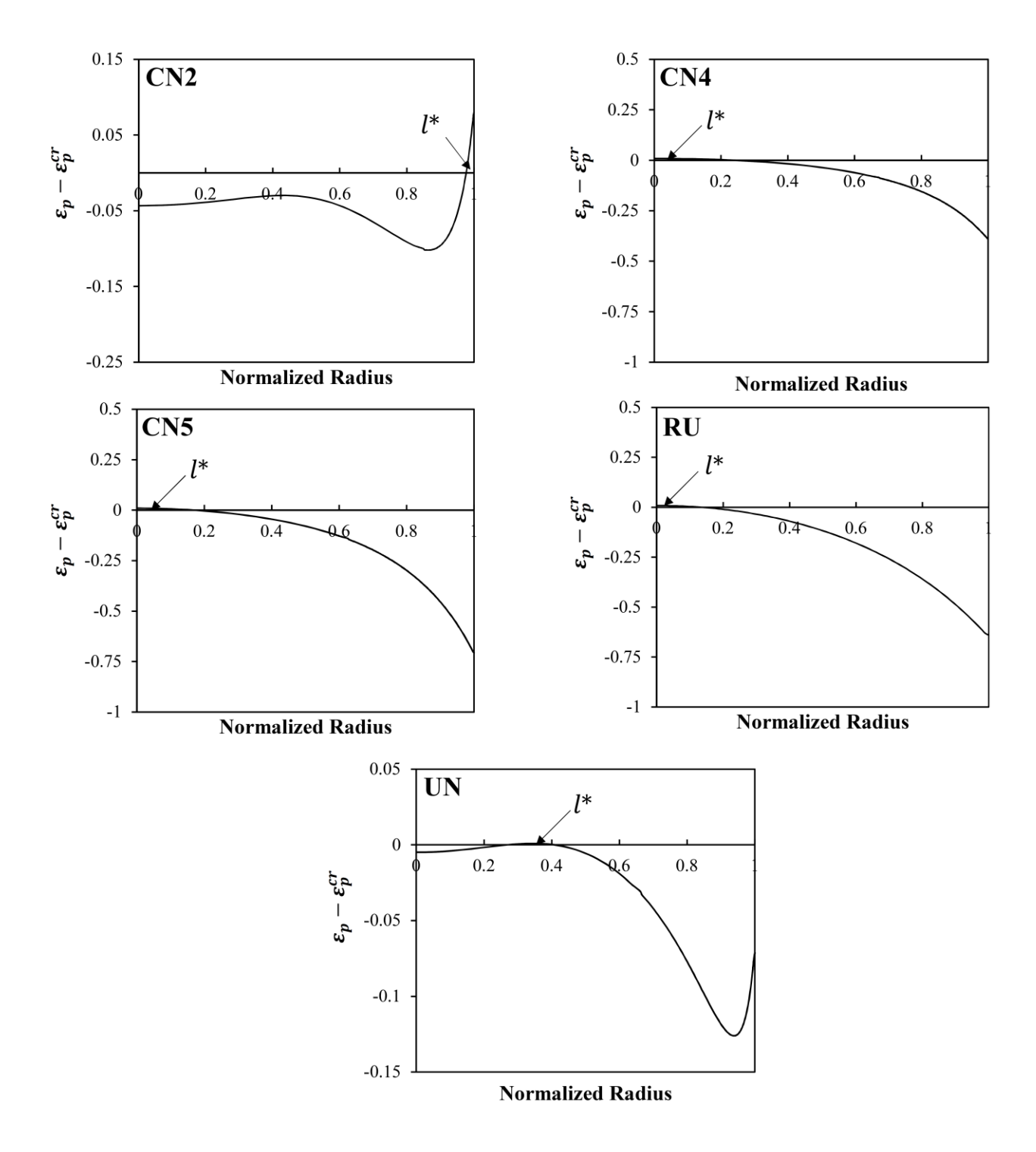


Figure 25: $(\varepsilon_p - \varepsilon_p^{cr})$ profiles of ASTM A992 steel fracture specimens